



# Correspondence-Attention Alignment for Multi-View Diffusion Models

Minkyung Kwon<sup>\*1</sup> Jinyeok Choi<sup>\*1</sup> Jiho Park<sup>\*1</sup>  
 Seonghu Jeon<sup>1</sup> Jinhyuk Jang<sup>1</sup> Junyoung Seo<sup>1</sup> Minseop Kwak<sup>1</sup>  
 Jin-Hwa Kim<sup>†2,3</sup> Seungryong Kim<sup>†1</sup>

<sup>1</sup>KAIST AI <sup>2</sup>NAVER AI Lab <sup>3</sup>SNU AIIS

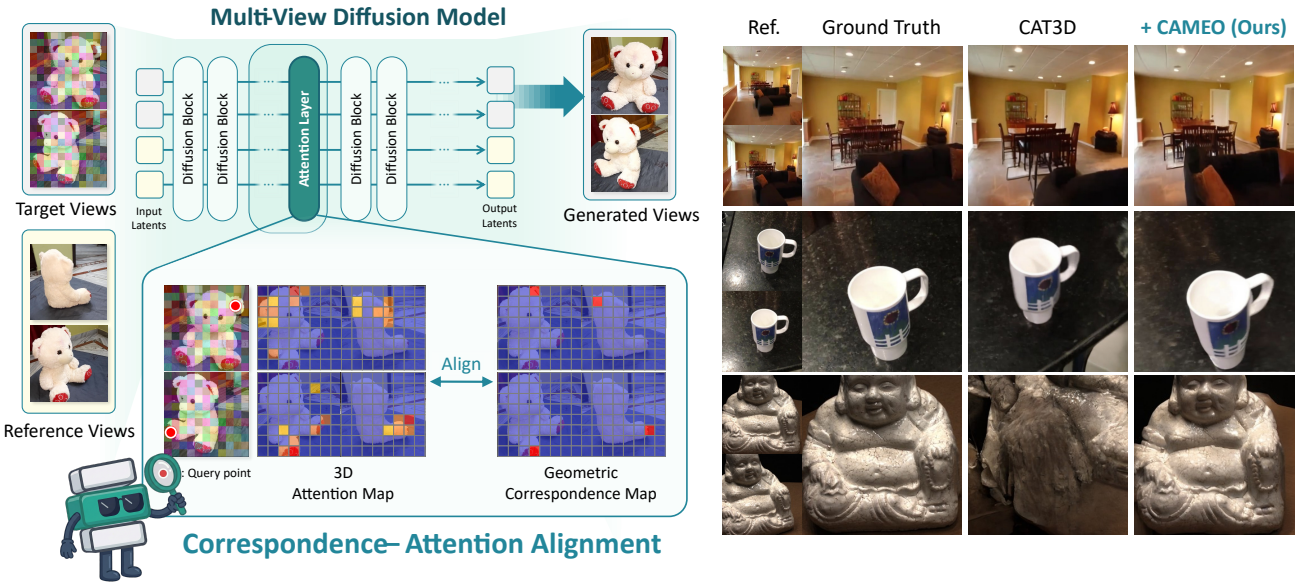


Figure 1. **Correspondence-attention alignment makes multi-view diffusion training effective.** Our framework, **CAMEO**, aligns attention maps of the multi-view diffusion models [6, 12, 26] with geometric correspondence. In experiments, CAMEO produces geometrically consistent novel views even in challenging scenarios involving large viewpoint changes or complex geometry.

## Abstract

Multi-view diffusion models have recently emerged as a powerful paradigm for novel view synthesis, yet the underlying mechanism that enables their view-consistency remains unclear. In this work, we first verify that the attention maps of these models acquire geometric correspondence throughout training, attending to the geometrically corresponding regions across reference and target views for view-consistent generation. However, this correspondence signal remains incomplete, with its accuracy degrading under large viewpoint changes. Building on these findings, we introduce **CAMEO**, a simple yet effective train-

ing technique that directly supervises attention maps using geometric correspondence to enhance both the training efficiency and generation quality of multi-view diffusion models. Notably, supervising a single attention layer is sufficient to guide the model toward learning precise correspondences, thereby preserving the geometry and structure of reference images, accelerating convergence, and improving novel view synthesis performance. CAMEO reduces the number of training iterations required for convergence by half while achieving superior performance at the same iteration counts. We further demonstrate that CAMEO is model-agnostic and can be applied to any multi-view diffusion model. Project page is available at <https://cvlab-kaist.github.io/CAMEO/>.

<sup>\*</sup>: Equal contribution

<sup>†</sup>: Co-corresponding author

## 1. Introduction

Novel view synthesis (NVS) is the task of predicting images from unseen viewpoints given reference views, preserving geometric consistency and photorealistic appearance. While optimization-based methods [20, 32] rely on per-scene optimization with dozens of input images, recent generative approaches, including multi-view diffusion models [6, 12, 28, 31, 39, 45, 50, 55], leverage generative priors from large-scale 2D diffusion models [14, 38] to synthesize novel views.

Multi-view diffusion models [6, 12, 40] employ 3D self-attention to aggregate information across viewpoints, where each query token from one view attends to all spatial locations across all views. As a result, they generate novel-view images that exhibit geometric consistency across views. However, as illustrated in Fig. 1, the consistency often deteriorates in challenging scenarios involving large viewpoint changes or complex geometry, leading to cross-view misalignment and structural degradation. These observations motivate a central question: *how do multi-view diffusion models maintain view-consistency through their internal mechanisms?*

In this work, we aim to understand the internal mechanisms governing geometric consistency in multi-view diffusion models [6, 12, 40] and leverage this understanding to improve their performance. To achieve this, we first analyze their 3D self-attention maps, yielding three key findings that motivate our method. (1) These models learn to encode geometric correspondences within their attention layers, and this emergent property concentrates in particular layers of the model. (2) The quality of this learned correspondence directly impacts the models’ performance: correspondence improves throughout training and correlates strongly with generation quality. (3) Yet, this correspondence signal is limited. A substantial precision gap remains compared to geometry prediction models (e.g. VGGT [48]), and the correspondence fails under large viewpoint rotations. These observations suggest that *while geometric correspondence is inherently learned within the attention layers of multi-view diffusion models, the signal remains incomplete and fragile.*

Our findings point to a promising direction: augment training with explicit geometric supervision to mitigate these limitations and enhance the synthesis quality. To this end, we introduce **CAMEO** (Correspondence–Attention Alignment for Multi-view Diffusion Models), a simple yet effective technique that supervises attention layers with geometric correspondence. We demonstrate that supervising a single attention layer is sufficient to improve both learning efficiency and performance.

CAMEO provides strong cues for geometrically consistent generation, resulting in faster convergence and higher-quality NVS. Notably, our method preserves geome-

try—generated images maintain accurate shapes consistent with the reference views, as illustrated in Fig. 1.

To evaluate the effectiveness, we conduct comprehensive experiments primarily based on CAT3D [12], evaluating on both scene-level [56] and object-centric [18, 37] datasets. CAMEO reduces the training iterations required for convergence by half, while achieving better performance at the same number of training iterations. To demonstrate its model-agnostic applicability, we further apply CAMEO to a state-of-the-art model [6], which utilizes geometric conditions, and a DiT-based [26] multi-view diffusion model, achieving consistent improvements across all frameworks.

The main contributions of this paper are as follows:

- We present an in-depth analysis of multi-view diffusion models, revealing that geometric correspondence emerges in attention maps during training and is critical for NVS performance.
- We propose CAMEO, a simple and effective technique that supervises the model’s attention maps with geometric correspondence.
- We demonstrate that our method enhances NVS performance across representative multi-view diffusion models [6, 12, 26], preserving geometry, accelerating convergence, and improving novel view synthesis performance.

## 2. Related work

**Diffusion models for novel view synthesis.** Diffusion models [14, 38] have recently emerged as powerful generative priors for novel view synthesis (NVS), advancing beyond traditional geometry-based approaches [20, 32]. Early methods [28, 39, 50] formulated NVS as a conditional image-to-image translation problem, predicting a single target view from one or more reference views. More recent multi-view diffusion frameworks synthesize sets of geometrically consistent views by extending 2D latent diffusion models with a 3D self-attention [12, 45, 55]. Building upon these, some methods further incorporate conditioning from geometry-prediction models [22, 31, 53].

We focus on analyzing the underlying mechanisms by which diffusion models internalize geometric cues, showing that correspondence in attention enables effective inference of geometry. We find that explicitly aligning attention with geometric correspondence further improves view-consistent generation.

**Learning feature representations by supervision.** Recent work improves diffusion models [4, 36, 38] by supervising their internal features with external signals. REPA [54] introduces feature-level supervision by distilling semantic features from DINOv2 [35] into early layers of a Diffusion Transformer (DiT) [36], accelerating convergence and enhancing semantic structure. Similarly, NVComposer [24] supervises the features using pointmaps obtained from a

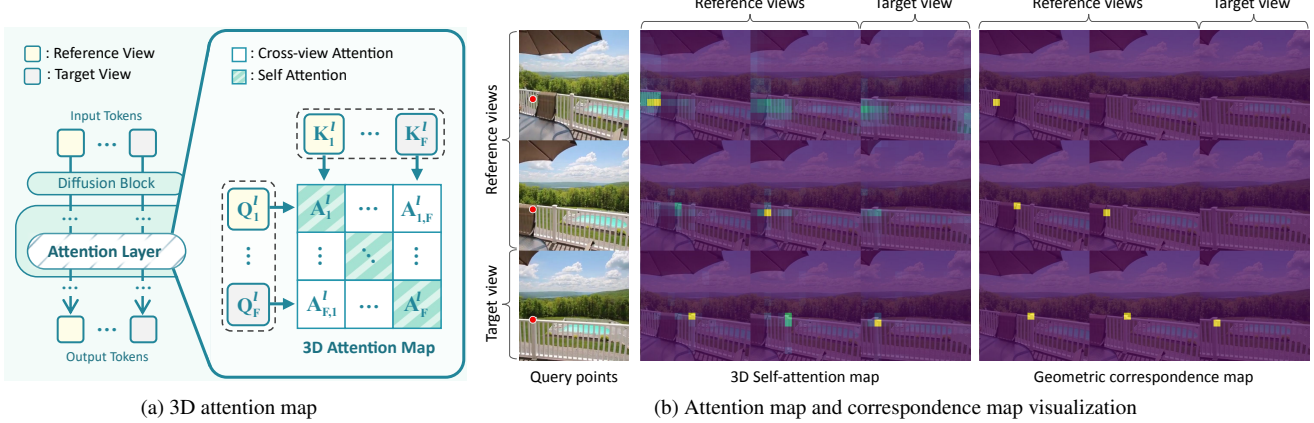


Figure 2. **Attention maps in multi-view diffusion models and geometric correspondence map:** (a) Multi-view diffusion models and their 3D self-attention maps [6, 12]. (b) Attention vs. geometric correspondence map. The attention map of layer  $l = 10$  in CAT3D [12] naturally focuses on its geometric counterpart across views even without explicit supervision.

dense stereo model [49], and Track4Gen [19] applies tracking supervision on the features to reduce appearance drift. Concurrently, Geometry Forcing [51] aligns diffusion features with geometry-aware embeddings from a pretrained geometry prediction model [48]. These methods show that structural or temporal priors can be encoded through feature alignment, yet the mechanism by which aligned features improve generation remains unclear.

Feature alignment enriches per-view semantics or geometry but does not enforce cross-view consistency [15]. In this work, we identify correspondence in attention as the key signal for consistency. By aligning attention maps rather than features [51, 54], we guide the model to attend to geometrically corresponding regions across views, enabling it to capture pose and spatial relationships that improve both consistency and generation quality.

**Attention mechanism in diffusion models.** Diffusion models commonly employ U-Net [38] and Transformer [36] architectures, whose attention mechanisms selectively integrate information across modalities, spatial locations, and temporal sequences, demonstrating an inherent understanding of spatial structure and geometry. In text-to-image diffusion models, attention maps link text prompts to specific spatial regions, allowing localized edits and geometric control [5, 7, 13, 34]. This spatial awareness extends to segmentation tasks, where attention accurately separates spatial components [44]. For video generation, temporal attention naturally encodes tracking information across frames [33], enabling the generation of motion-realistic videos by capturing object and scene geometry. These observations reveal that attention carries structured spatial and temporal signals. Extending this principle to multi-view settings, we study attention in multi-view diffusion models as a carrier of geometric correspondence across views and introduce explicit supervision to reinforce this correspondence for improved view consistency.

### 3. Method

In the following sections, we first provide preliminaries on multi-view diffusion models (Sec. 3.1). We then analyze the attention maps of multi-view diffusion models (Sec. 3.2). Motivated by the findings in our analysis, we propose **CAMEO**, which accelerates the learning of accurate cross-view relationships and improves novel view synthesis quality (Sec. 3.3).

#### 3.1. Preliminaries

The goal of novel view synthesis (NVS) is to generate  $M$  target images  $\{\mathbf{I}_i^{\text{tgt}}\}_{i=1}^M$  for target camera poses  $\{\boldsymbol{\pi}_i^{\text{tgt}}\}_{i=1}^M$ , given  $N$  reference images  $\{\mathbf{I}_i^{\text{ref}}\}_{i=1}^N$  and their corresponding camera poses  $\{\boldsymbol{\pi}_i^{\text{ref}}\}_{i=1}^N$ .

Multi-view diffusion models [6, 12, 40, 55] built upon pretrained text-to-image diffusion models [26, 38] typically employ a 3D self-attention mechanism. Specifically, they extend the standard 2D attention in pretrained text-to-image diffusion models by concatenating the token sequences from each view, allowing features to interact both within and across views. Given  $N$  reference views and  $M$  target views, we set the number of total views to  $F = N + M$ . At diffusion timestep  $t$  and attention layer  $l$  of a multi-view diffusion model, features from each of the  $F$  images are projected into query ( $\mathbf{Q}_i^{l,t}$ ) and key ( $\mathbf{K}_i^{l,t}$ ) matrices for view  $i \in \{1, \dots, F\}$ , each of size  $\mathbb{R}^{h w \times d}$ , where  $h$  and  $w$  denote the height and width of the feature map, and  $d$  is the embedding dimension of each token. These are then concatenated along the spatial axis, stacking tokens from all  $F$  views into a single sequence, with  $N$  reference views followed by  $M$  target views. This produces the final query and key matrices,  $\mathbf{Q}^{l,t}$  and  $\mathbf{K}^{l,t}$ , each of size  $\mathbb{R}^{F h w \times d}$ . The 3D attention map  $\mathbf{A}^{l,t} \in \mathbb{R}^{F h w \times F h w}$  is then computed via scaled dot-product attention with row-wise softmax,  $\text{softmax}(\cdot)$ . For notational simplicity, we omit the timestep notation and write  $\mathbf{A}^l$  henceforth.

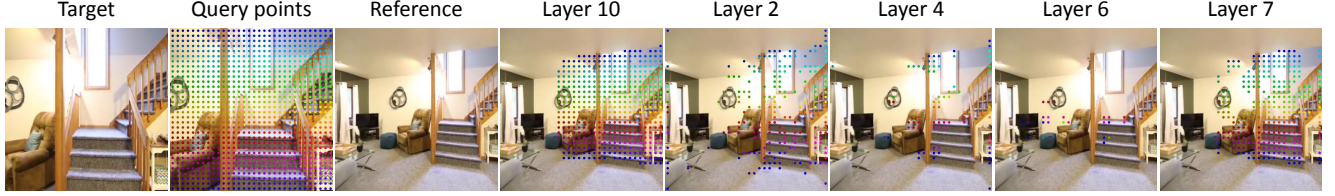


Figure 3. **Layer-wise behavior of the multi-view diffusion model (CAT3D [12])’s attention map.** For each query point on the target image, model’s maximum attending point in the reference image is marked with the same color as the query point. Attention map of layer  $l = 10$  clearly attends to geometrically corresponding point, while other layers do not. We fix a timestep  $t = 999$  (*i.e.*, complete noise).

As shown in Fig. 2a, the 3D self-attention map can be categorized into two key interactions: (1) self-attention  $\mathbf{A}_i^l$ , (2) cross-view attention  $\mathbf{A}_{i,j}^l$ , where  $i, j \in \{1, \dots, F\}$  with  $i \neq j$ . Of these, cross-view attention  $\mathbf{A}_{i,j}^l \in \mathbb{R}^{hw \times hw}$  is of particular interest to our study. For each query token at index  $\mathbf{x}_i \in \{1, \dots, hw\}$  in  $\mathbf{Q}_i^l$ ,  $\mathbf{A}_{i,j}^l(\mathbf{x}_i) \in \mathbb{R}^{hw}$  represents a probability distribution of attention weights over all key tokens in  $\mathbf{K}_j^l$ . This mechanism is particularly important as it enables each spatial location in one view to aggregate information from any location in other views. For our analysis and our method, we compute the normalized cross-view attention map  $\mathbf{A}_{i,j}^l = \text{softmax}(\mathbf{Q}_i^l(\mathbf{K}_j^l)^\top / \sqrt{d})$  for each view pair  $(i, j)$  with  $i \neq j$ .

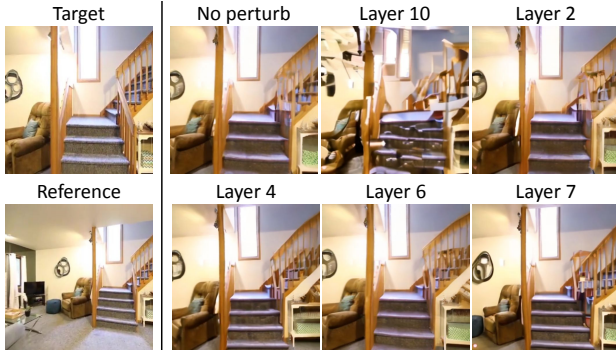


Figure 4. **Effect of layer-wise attention perturbation.** Following the perturbation procedure of PAG [1], perturbing earlier layers barely changes generation quality, while perturbing layer 10 collapses geometric consistency and severely degrades quality.

### 3.2. Motivation and analysis

We begin by qualitatively analyzing the layer-wise behavior of the cross-view attention maps. Specifically, given two images  $\mathbf{I}_1$  (target) and  $\mathbf{I}_2$  (reference) of the same scene from different viewpoints, we first obtain query  $\mathbf{Q}_1^l$  and key  $\mathbf{K}_2^l$  during the denoising process to compute the cross-view attention map  $\mathbf{A}_{1,2}^l$ . For each query token index  $\mathbf{x}_1$  in  $\mathbf{Q}_1^l$ , we identify the key token index with the highest attention weight. As shown in Fig. 3, layer  $l = 10$  exhibits a consistent pattern: a query token consistently attends to its geometrically corresponding point in another view. This observation leads us to hypothesize that the cross-view attention

maps in the model capture geometric correspondence. We provide the visualization results for all layers in Sec. C.1.

To rigorously investigate and understand this emergent behavior, we quantitatively measure the geometric correspondence encoded in the attention maps [2]. Following Probe3D [11], which proposed a framework to evaluate semantic or geometric correspondence, we evaluate the geometric correspondence within the cross-view attention map of the multi-view diffusion model [12]. Specifically, given an image pair  $\mathbf{I}_1$  and  $\mathbf{I}_2$  with a viewpoint rotation angle  $\theta$  from the NAVI dataset [17], we estimate the correspondence for each query point of  $\mathbf{I}_1$  with another image  $\mathbf{I}_2$  by identifying the location with the highest attention weight in  $\mathbf{A}_{1,2}^l$ . We also evaluate the baselines, including (i) the attention map of CAT3D before finetuning, (SD2.1 [38]-initialized, denoted SD2.1), (ii) the dense SIFT descriptors (DSIFT) from SIFT Flow [27], (iii) the intermediate features of DINOv3-L [41], and (iv) the point maps from VGGT [48]. We summarize the evaluation results in Fig. 5 and provide details in Sec. C.2.

**Emergence of geometric correspondence in attention layers.** As shown in Fig. 5a, we report the geometric correspondence precision averaged over all viewpoint rotations ( $\theta$ ) for layers  $l = 2, 4, 6, 7, 10$ , which are the first layers of each U-Net block. Compared to SD2.1 [38], CAT3D [12] develops significantly stronger correspondence in its cross-view attention maps in layers  $l = 7, 10$  that outperform DSIFT [27]. In particular, layer  $l = 10$  achieves precision comparable to DINOv3-L [41]. For  $l = 10$ , the precision for each viewpoint rotation angle is given in Fig. 5b. For small viewpoint rotation,  $\theta = 0^\circ - 30^\circ$ , CAT3D achieves as high a precision as VGGT [48] pointmaps, demonstrating its ability to capture geometric correspondence.

**Geometric correspondence improves throughout training.** In Fig. 5c, we plot the geometric correspondence precision in  $l = 10$  across training iterations in CAT3D [12]. We observe that both the correspondence precision and PSNR increase monotonically during training, demonstrating that the model progressively learns to encode more accurate geometric correspondence in the attention map. This positive correlation between correspondence precision and generation quality suggests that this correspondence underpins the

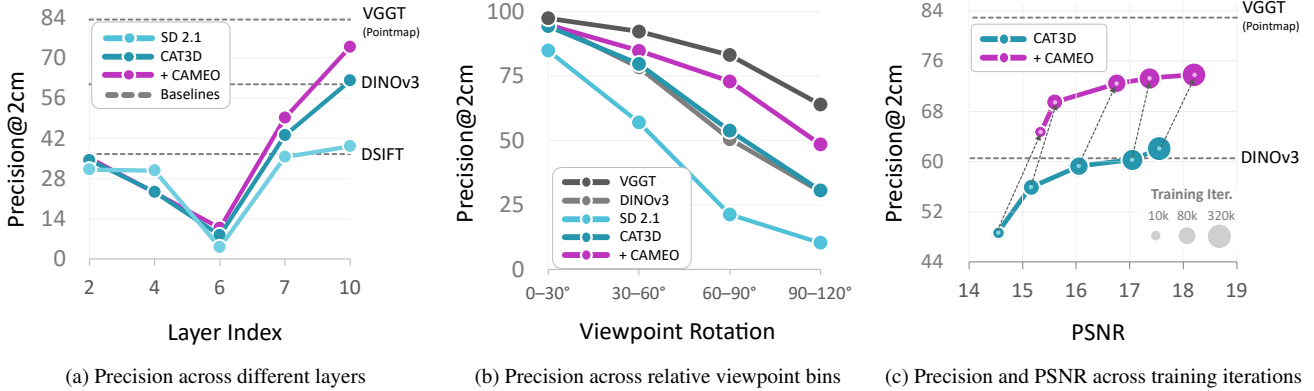


Figure 5. **Analysis of geometric correspondence in attention maps of the multi-view diffusion model [12].** (a) Correspondence precision across attention layers ( $l = 2, 4, 6, 7, 10$ ), with other baselines [27, 38, 41, 48]. (b) The correspondence precision of layer  $l = 10$  with baselines, across viewpoint rotation. (c) The correspondence precision of layer  $l = 10$  improves during training.

synthesis quality. We further verify this in Fig. 4 by perturbing its attention map. Following PAG [1], we force the 3D self-attention at a given layer to an identity mapping so that each query only attends to its corresponding identity location. Perturbing earlier layers (e.g.,  $l = 2, 4, 6, 7$ ) leaves the outputs nearly unchanged, whereas perturbing  $l = 10$  collapses the scene into a heavily distorted, geometrically implausible image. This demonstrates that the ability of  $l = 10$  to capture geometric correspondences across views is crucial for view-consistent generation.

**Denoising objectives provide limited correspondence supervision.** Although the attention layers capture geometric correspondence and their precision correlates with the generation quality, a substantial performance gap remains compared to a strong baseline, VGGT [48]. As shown in Figs. 5a and 5c, CAT3D’s attention maps exhibit significantly lower correspondence precision than VGGT, even after extensive training iterations. More critically, Fig. 5b reveals that CAT3D’s attention maps struggle to capture accurate geometric correspondence under large viewpoint rotations, while VGGT maintains relatively robust performance across varying viewpoints. This suggests that the standard denoising objective alone is insufficient for the model to learn accurate geometric correspondence, motivating our exploration of explicit correspondence supervision.

### 3.3. CAMEO: Correspondence-attention alignment for multi-view diffusion models

We propose CAMEO, correspondence-attention alignment for multi-view diffusion models, which explicitly supervises the attention maps with the geometric correspondence. Our analysis (Sec. 3.2) shows that layer  $l = 10$  captures the strongest geometric correspondence and that its precision correlates with generation quality, yet it degrades significantly under large viewpoint rotation, indicating room for improvement. By directly supervising  $l = 10$  with geometric correspondence, we enable faster learning of geometric relationships and improved novel view synthesis.

**Geometric correspondence map.** Given a set of images  $\{\mathbf{I}_i\}_{i=1}^F$ , dense geometric correspondence identifies matching pixels between any image pair  $(\mathbf{I}_i, \mathbf{I}_j)_{i \neq j}$  such that the matched pixels correspond to the same point in the 3D space. These correspondences can be aligned to the token-level resolution  $h \times w$  through spatial downsampling or interpolation. Specifically, the geometric correspondences for all  $\mathbf{x}_i$  can be defined as  $\{(\mathbf{x}_i, \mathbf{x}_j), \mathbf{M}_{i,j}(\mathbf{x}_i)\}^{hw}$ , where  $\mathbf{x}_i, \mathbf{x}_j \in \{1, \dots, hw\}$  are the query token indices and  $\mathbf{M}_{i,j}(\mathbf{x}_i) \in [0, 1]$  is a visibility mask, indicating whether the corresponding point of  $\mathbf{x}_i$  is visible in  $\mathbf{I}_j$ .

Then we build a one-hot correspondence vector  $\mathbf{P}_{i,j}(\mathbf{x}_i) \in \mathbb{R}^{hw}$  for each  $\mathbf{x}_i$ , where its  $\mathbf{x}_j$ -th element is 1 while others are all zero. We then stack these vectors over all query token indices  $\mathbf{x}_i$  to get a geometric correspondence map  $\mathbf{P}_{i,j} \in \mathbb{R}^{hw \times hw}$ . We construct such maps for all pairs among the  $N$  reference and  $M$  target images.

We follow DUS3R [49] to obtain the correspondences from pointmaps by finding the nearest neighbor in 3D space. To compute  $\mathbf{M}_{i,j}$ , we verify cycle correspondence consistency. For a query token index  $\mathbf{x}_i$ , we obtain the cycle correspondence index  $\hat{\mathbf{x}}_i$  using correspondences  $(\mathbf{x}_i, \mathbf{x}_j)$  and  $(\mathbf{x}_j, \hat{\mathbf{x}}_i)$ . We convert the flattened token indices to their corresponding 2D spatial coordinates and set  $\mathbf{M}_{i,j}(\mathbf{x}_i) = 1$  only when  $\|\mathbf{p}(\mathbf{x}_i) - \mathbf{p}(\hat{\mathbf{x}}_i)\|_2 \leq \tau$ , where  $\mathbf{p}(\cdot)$  denotes the mapping from token index to 2D spatial coordinate and  $\tau$  is a cycle consistency threshold.

**Correspondence-attention alignment.** Our method simply aligns the cross-view attention map  $\mathbf{A}_{i,j}^l \in \mathbb{R}^{hw \times hw}$  with the geometric correspondence map  $\mathbf{P}_{i,j} \in \mathbb{R}^{hw \times hw}$  for all view pairs and query tokens. In Fig. 2b, we visualize the cross-view attention map  $\mathbf{A}_{i,j}^l(\mathbf{x}_i)$  and geometric correspondence map  $\mathbf{P}_{i,j}(\mathbf{x}_i)$  for a query token index  $\mathbf{x}_i$  of each view  $i$ . In practice, multi-view diffusion models typically employ multi-head attention [6, 12, 28, 31, 39, 45, 50, 55], allowing different heads to capture diverse patterns and representations. Applying uniform alignment across all heads would restrict the architectural flexibility and limit the

model’s expressive capacity. To mitigate this, we employ a projection head on the attention logits before  $\text{softmax}(\cdot)$ , using a simple multilayer perceptron (MLP).

We define the CAMEO loss on a layer  $l$ :

$$\mathcal{L}_{\text{CAMEO}} = \mathbb{E}_{(i,j), \mathbf{x}_i} [\mathbf{M}_{i,j}(\mathbf{x}_i) \odot \text{CE}(\mathbf{A}_{i,j}^l(\mathbf{x}_i), \mathbf{P}_{i,j}(\mathbf{x}_i))] \quad (1)$$

where  $\text{CE}(\cdot)$  is the cross-entropy loss, and  $\odot$  denotes element-wise multiplication.

**Training objective.** Our final training objective combines the standard denoising score matching loss  $\mathcal{L}_{\text{denoise}}$  used in diffusion models [14] with the proposed correspondence-attention alignment loss as  $\mathcal{L}_{\text{total}} = \mathcal{L}_{\text{denoise}} + \lambda \mathcal{L}_{\text{CAMEO}}$ , where  $\lambda$  is a hyperparameter.

## 4. Experiments

We evaluate the effectiveness of **CAMEO** by addressing the following key questions:

- Does CAMEO improve the quality of novel view synthesis under large viewpoint changes and complex scene?
- Can CAMEO accelerate the training of multi-view diffusion models?
- Does CAMEO remain effective under out-of-domain (OOD) settings, demonstrating generalization beyond the training distribution?
- Is CAMEO a general framework, which can be applied to any multi-view diffusion models?

### 4.1. Setup

**Model.** We adopt CAT3D [12] as the baseline multi-view diffusion model for our main experiments. Since the official implementation of CAT3D is not publicly available, we employ the re-implementation provided by MVGenMaster [6]. Following prior works [12, 28], we initialize the model from pretrained Stable Diffusion 2.1 weights [38]. Additional architectural details are provided in Sec. B. For comparison, we also train and evaluate two baseline methods: (1) REPA [54], a feature alignment method using self-supervised model [35] features, and (2) Geometry Forcing [51], a feature alignment method that aligns diffusion features with geometric features extracted from a geometric prediction model [48].

To verify that CAMEO generalizes beyond our baseline architecture [12], we further implement CAMEO in two additional architectures: MVGenMaster [6], a state-of-the-art multi-view diffusion model that adopts geometric conditioning, and a DiT-based [26] multi-view diffusion model. Implementation details for these models are provided in Sec. D.3.

**Dataset.** For the main experiments, we train the models on the scene-level (RealEstate10K [56]) and object-centric (CO3D [37]) datasets separately to demonstrate that our method is applicable to both scene-level and object-level

synthesis. Each training sample consists of  $F = 4$  views, where 1 to 3 views are randomly masked as target views while the rest as references. For the main evaluation, we measure the performance under two settings: one reference view with three target views (1-to-3) and two reference views with two target views (2-to-2), covering a diverse range of camera poses. We randomly sample 280 scenes from the RealEstate10K test set [56] and 240 scenes from the CO3D test set [37], evaluating models trained on their respective datasets. For an out-of-domain (OOD) evaluation, we evaluate the scene-level model on the validation split of the DTU dataset (object-centric) [18], processed by MVsplat [8], and we conduct evaluation under 2-to-2 view setting. All models are trained and evaluated at  $512 \times 512$  resolution.

**Geometric correspondence map.** We use off-the-shelf geometry model [48] to get pointmaps and bilinearly interpolate them to compute token-level geometric correspondence. We provide the details, including computation cost in Sec. D.2.

**Implementation details.** In the main experiments, we apply CAMEO to layer  $l = 10$ , which shows the strongest emergent correspondence among all layers, yet the correspondence degrades significantly under large viewpoint rotations (Sec. 3.2). We set a loss weight  $\lambda = 0.02$ , and the cycle consistency threshold  $\tau = 1.5$ . For REPA [54], we apply the REPA loss  $\mathcal{L}_{\text{REPA}}$  to  $l = 3$  with a loss weight of 0.5, following the observation in the original paper. For Geometry Forcing [51], we apply the angular alignment loss  $\mathcal{L}_{\text{Angular}}$  and the scale alignment loss  $\mathcal{L}_{\text{Scale}}$  at layer  $l = 3$  using VGGT [48] features, with a loss weight of 0.5.

For MVGenMaster [6], we apply CAMEO at layer  $l = 10$  since it has the same UNet architecture as CAT3D [12]. For the DiT-based model [26], we apply CAMEO at  $l = 32$ , identified by our analysis as the layer capturing the strongest geometric correspondence. We provide the detailed analysis of the DiT-based model in Sec. C.3.

**Training details.** We keep the batch size to 6 and train models with AdamW optimizer [29], adopting a fixed learning rate of 2.5e-5 and a weight decay of 0.01. Following [6, 12], we apply classifier-free guidance (CFG) [9] training by randomly dropping camera condition with a probability of 0.1. At inference, we use the DDIM sampler [42] with 50 sampling steps and CFG with a weight of 2.0. All experiments are conducted on 2 NVIDIA A100 (40GB) GPUs.

### 4.2. Main results

**Training efficiency.** To investigate how CAMEO influences the training dynamics of multi-view diffusion models, we compare CAMEO with the baseline at intermediate training steps. As shown in Tab. 1, our method achieves faster convergence than the baseline [12] and REPA [54]. Specifically, CAMEO reaches a PSNR above 19.4 at 80k



Figure 6. **Qualitative results** on (a) RealEstate10K [56]. (b) CO3D [37], (c) DTU [18] (Out-of-domain). CAMEO accelerates learning of pose and geometric relationships compared to the baseline, as explicit correspondence supervision encourages geometric consistency and faster convergence in novel view synthesis. Additional results are provided in Sec. F.

iterations, whereas the baseline requires 160k or more iterations to achieve the same performance — corresponding to a  $2\times$  acceleration. These results demonstrate that CAMEO enables more efficient learning of geometric structure in multi-view diffusion models.

**Novel view synthesis quality.** The benefits of CAMEO extend beyond training efficiency to improvements in the final quality of novel view synthesis. As shown in Tab. 1, CAMEO surpasses both the baseline [12], REPA [54], and Geometry Forcing [51] at nearly all intermediate training iterations. These results indicate that aligning attention to a specific layer yields larger gains than feature-level alignment. Importantly, CAMEO consistently outperforms the baseline after convergence (beyond 320k iterations), demonstrating that it not only accelerates training but also improves final performance. Furthermore, Fig. 6 demonstrates that CAMEO produces novel views that are more aligned with the ground-truth images and better preserve

object structure compared to the baseline. Specifically, in Fig. 6c, CAMEO captures the overall geometric structure of the building and brick as early as 40k iterations, whereas the baseline fails to recover these appearances. Even after 320k iterations, the baseline [12] still struggles to accurately generate the building’s roof and brick details, while CAMEO generates them with high geometric consistency. These results confirm that explicit correspondence supervision significantly improves overall NVS quality. Additional qualitative examples are provided in Sec. F.

**Generalization to OOD setting.** The advantages of CAMEO are not limited to in-domain settings. As shown in Tab. 1, even when evaluated on the object-centric DTU dataset [18], our method consistently outperforms the baseline. This suggests that CAMEO enables the model to learn a general geometric understanding that extends beyond the training distribution.

**Generalization to other architectures.** We also evaluate

Table 1. Novel view synthesis evaluation on RealEstate10K [56], CO3D [37], and DTU [18]. **Bold** numbers indicate the best within each iteration group.

Model	Iter.	RealEstate10K [56]			CO3D [37]			DTU [18] (Out-of-domain)		
		PSNR $\uparrow$	SSIM $\uparrow$	LPIPS $\downarrow$	PSNR $\uparrow$	SSIM $\uparrow$	LPIPS $\downarrow$	PSNR $\uparrow$	SSIM $\uparrow$	LPIPS $\downarrow$
CAT3D [12] w/ REPA [54] w/ Geometry Forcing [51] w/ CAMEO (Ours)	10k	16.68	0.617	0.377	14.55	<b>0.555</b>	0.560	9.35	0.285	0.603
		16.82	0.613	0.379	14.24	0.542	0.558	9.81	0.296	0.607
		17.71	0.648	0.362	14.11	0.521	0.549	9.47	0.303	0.604
		<b>18.00</b>	<b>0.650</b>	<b>0.346</b>	<b>15.33</b>	0.548	<b>0.521</b>	<b>9.99</b>	<b>0.311</b>	<b>0.589</b>
CAT3D [12] w/ REPA [54] w/ Geometry Forcing [51] w/ CAMEO (Ours)	40k	18.13	0.650	0.330	15.16	0.557	0.531	9.90	0.308	0.603
		18.27	0.654	0.325	<b>15.69</b>	0.560	<b>0.507</b>	10.45	0.342	0.580
		18.49	<b>0.670</b>	0.328	15.10	0.529	0.512	9.89	<b>0.345</b>	0.598
		<b>18.56</b>	0.667	<b>0.315</b>	15.60	<b>0.566</b>	0.513	<b>10.76</b>	0.322	<b>0.552</b>
CAT3D [12] w/ REPA [54] w/ Geometry Forcing [51] w/ CAMEO (Ours)	80k	18.99	0.682	0.317	16.05	0.570	0.495	10.29	0.321	0.574
		18.70	0.672	0.312	16.10	0.573	0.495	10.31	0.353	0.585
		18.92	0.676	0.316	15.94	0.563	0.484	10.43	0.344	0.587
		<b>19.40</b>	<b>0.690</b>	<b>0.301</b>	<b>16.76</b>	<b>0.589</b>	<b>0.478</b>	<b>11.45</b>	<b>0.387</b>	<b>0.531</b>
CAT3D [12] w/ REPA [54] w/ Geometry Forcing [51] w/ CAMEO (Ours)	160k	19.28	0.686	0.300	17.05	0.579	<b>0.456</b>	10.49	0.321	0.588
		19.42	0.698	0.292	16.78	0.584	0.468	11.72	<b>0.385</b>	<b>0.522</b>
		19.24	0.685	0.305	16.91	0.574	0.458	11.69	0.373	0.554
		<b>19.51</b>	<b>0.699</b>	<b>0.288</b>	<b>17.37</b>	<b>0.591</b>	<b>0.456</b>	<b>12.06</b>	0.353	0.526
CAT3D [12] w/ REPA [54] w/ CAMEO (Ours)	320k	19.88	0.702	0.287	17.55	0.601	0.448	<b>12.23</b>	<b>0.401</b>	0.524
		19.76	0.702	0.286	17.61	0.603	0.453	11.71	0.365	<b>0.521</b>
		<b>20.16</b>	<b>0.716</b>	<b>0.279</b>	<b>18.20</b>	<b>0.608</b>	<b>0.425</b>	12.16	0.380	0.526
CAT3D [12] w/ REPA [54] w/ CAMEO (Ours)	400k	19.64	0.696	0.293	17.06	0.580	0.446	11.16	0.337	0.588
		19.96	0.709	0.283	17.09	0.580	0.445	10.92	0.365	0.561
		<b>20.07</b>	<b>0.710</b>	<b>0.277</b>	<b>17.74</b>	<b>0.603</b>	<b>0.426</b>	<b>12.58</b>	<b>0.402</b>	<b>0.493</b>

CAMEO on the other baseline architectures, a state-of-the-art [6] and a DiT-based model [26]. As shown in Tabs. 4 and 5, CAMEO yields improvements in PSNR, SSIM, and LPIPS across both models, particularly in early training iterations. These results demonstrate that our framework improves multi-view diffusion models with varying architectures, confirming its model-agnostic nature. We provide qualitative results of both models in Sec. F.

#### 4.3. Ablation studies

To analyze the contribution of each component in CAMEO, we conduct comprehensive ablation studies by systematically varying its core components: the alignment layer, the presence of an MLP head, the weighting parameter  $\lambda$ , the

loss function, and the cycle consistency threshold  $\tau$ . All models are trained on the RealEstate10K dataset [56] with a batch size of 3 and evaluated in a 2-to-2 view setting.

Tab. 3 presents our alignment layer analysis. While supervising intermediate layers ( $l = 4, 6, 7$ ) yields poor performance, layer  $l = 10$  demonstrates competitive performance with  $l = 2$  at 40k iterations and clearly outperforms it by 80k iterations, validating our analysis in Sec. 3.2.

As shown in Tab. 2, incorporating an MLP head proves superior to direct alignment, as it preserves the representational diversity of multi-head attention. We find that  $\lambda = 0.02$  (balancing loss magnitudes) and  $\tau = 1.5$  (ensuring reliable matches) yield optimal results. Furthermore, cross-entropy loss achieves superior performance compared to L1 loss, as it directly aligns attention probability distributions.

#### 4.4. Analysis

We analyze the effect of CAMEO by measuring correspondence precision and visualizing the attention maps of CAT3D [12] trained with and without CAMEO.

**Correspondence accuracy.** Fig. 5 presents two observations. In Figs. 5a and 5b, CAMEO increases attention correspondence precision across all viewpoint rotations, even surpassing feature matching in DINOv3 [41]. As shown in Fig. 5c, CAMEO can push the baseline [12] to achieve both higher correspondence precision and PSNR at the same iterations, indicating faster learning of geometric correspondence and earlier gains in generation quality.

Table 2. Ablation studies of CAMEO on RealEstate10K [56]. All at 40k iterations.

Part	Factors	Variants	PSNR $\uparrow$	SSIM $\uparrow$	LPIPS $\downarrow$
(a)	MLP head	$\times$	18.08	0.653	0.343
		$\checkmark$	<b>18.31</b>	<b>0.658</b>	<b>0.337</b>
(b)	Loss weight ( $\lambda$ )	0.01	18.22	0.657	0.351
		<b>0.02</b>	18.31	<b>0.658</b>	<b>0.337</b>
		0.03	<b>18.37</b>	0.656	0.377
(c)	Loss type	L1	17.84	0.641	0.342
		<b>CE(-)</b>	<b>18.31</b>	<b>0.658</b>	<b>0.337</b>
(d)	Consistency threshold ( $\tau$ )	$\infty$	18.18	0.656	0.341
		3	17.49	0.648	0.338
		<b>1.5</b>	<b>18.31</b>	<b>0.658</b>	<b>0.337</b>

Table 3. **Layer Ablation.** **Bold** numbers indicate the best within each iteration group.

Layer	Iter.	PSNR↑	SSIM↑	LPIPS↓
2		18.26	<b>0.664</b>	<b>0.336</b>
4		17.98	0.653	0.343
6	40k	17.84	0.645	0.342
7		18.07	0.648	0.339
<b>10</b>		<b>18.31</b>	0.658	0.337
2		18.80	0.676	<b>0.315</b>
4		18.78	0.673	0.320
6	80k	18.19	0.663	0.326
7		18.60	0.666	0.323
<b>10</b>		<b>19.08</b>	<b>0.681</b>	0.316

Table 4. **CAMEO on MVGenMaster [6].** **Bold** numbers indicate the best within each iteration group.

Model	Iter.	PSNR↑	SSIM↑	LPIPS↓
MVGenMaster [6]		17.35	0.649	0.327
w/ CAMEO (Ours)	20k	<b>18.31</b>	<b>0.671</b>	<b>0.315</b>
MVGenMaster [6]		18.64	0.682	0.306
w/ CAMEO (Ours)	40k	<b>18.70</b>	<b>0.668</b>	<b>0.305</b>
MVGenMaster [6]		18.84	0.678	0.305
w/ CAMEO (Ours)	60k	<b>19.21</b>	<b>0.695</b>	<b>0.304</b>
MVGenMaster [6]		19.45	0.699	0.295
w/ CAMEO (Ours)	120k	<b>19.56</b>	<b>0.700</b>	<b>0.292</b>

Table 5. **CAMEO on Hunyuan-DiT [26]** **Bold** numbers indicate the best within each iteration group.

Model	Iter.	PSNR↑	SSIM↑	LPIPS↓
Hunyuan-DiT [26]		14.40	0.533	0.459
w/ CAMEO (Ours)	20k	<b>16.17</b>	<b>0.575</b>	<b>0.373</b>
Hunyuan-DiT [26]		17.00	0.594	0.321
w/ CAMEO (Ours)	40k	<b>17.57</b>	<b>0.612</b>	<b>0.294</b>
Hunyuan-DiT [26]		17.55	0.610	0.289
w/ CAMEO (Ours)	60k	<b>18.52</b>	<b>0.639</b>	<b>0.260</b>
Hunyuan-DiT [26]		19.30	0.661	0.218
w/ CAMEO (Ours)	120k	<b>19.75</b>	<b>0.677</b>	<b>0.211</b>

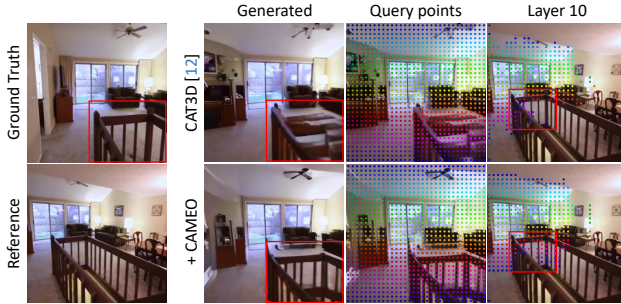


Figure 7. **Correspondence analysis in  $l = 10$ .** In CAT3D [12], pink query points on the handrail fail to attend to their geometric counterparts in the reference, whereas CAMEO succeeds. As a result, the handrail is accurately generated only in CAMEO.

**Qualitative analysis.** In Fig. 7, CAT3D [12] produces a distorted handrail, while CAMEO preserves the correct shape with fine detail and accuracy. The attention maps reveal the mechanism behind this performance gap. For CAT3D [12], query points on the handrail fail to attend to the handrail region in the reference image. In contrast, CAMEO correctly attends to the corresponding handrail region, resulting in precise geometric reconstruction with structural details. This demonstrates that CAMEO successfully guides the model to learn more accurate geometric correspondences, which directly improves novel view synthesis performance.

## 5. Conclusion

In this work, we presented an analysis of multi-view diffusion models, revealing that their 3D self-attention maps learn emergent geometric correspondence that is critical for generation quality. We also identified the limitations of this implicit signal, which proved fragile under large viewpoint changes. Building on these findings, we introduced CAMEO, a simple yet effective technique that injects explicit geometric supervision into the attention layers. We demonstrated that our approach significantly improves novel view synthesis quality, enhances geometric

fidelity under challenging viewpoints, and accelerates the training. CAMEO is model-agnostic and can be readily integrated into existing and future architectures that employ cross-view attention. We hope our findings on the link between the correspondence and the attention inspire further research in geometry-aware generative modeling.

## Appendix

This appendix presents additional experimental results and further details of our proposed method, CAMEO.

- Sec. A reviews the fundamentals of diffusion models.
- Sec. B describes the architecture of multi-view diffusion models in detail.
- Sec. C provides a detailed analysis of correspondence in multi-view diffusion models, including the analysis setup.
- Sec. D covers implementation details, including correspondence map derivation, and implementation of baseline models.
- Sec. E shows additional ablation studies.
- Sec. F presents additional qualitative results.
- Sec. G provides the results and implementation details of 3D reconstruction.
- Sec. H describes the limitations of CAMEO.
- Sec. I discusses future directions.

### A. Preliminaries for diffusion models

Diffusion models [14, 42] are a class of generative models that learn data distributions by reversing a gradual noising process. Starting from clean data samples  $x_0 \sim p_{\text{data}}(x)$ , a forward process incrementally corrupts them with Gaussian noise to produce a sequence of latent variables  $\{x_t\}_{t=1}^T$ . A neural network is then trained to approximate the reverse process, progressively denoising a sample from pure Gaussian noise back into a realistic data point.

**Denoising diffusion probabilistic models.** Denoising Diffusion Probabilistic Models (DDPM) [14] define a forward noising process  $q(x_t|x_{t-1})$  with a variance schedule  $\{\beta_t\}_{t=1}^T$ , where  $\alpha_t = 1 - \beta_t$  and  $\bar{\alpha}_t = \prod_{s=1}^t \alpha_s$ . At an arbitrary timestep  $t$ , the closed form of the noising process is

$$x_t = \sqrt{\bar{\alpha}_t} x_0 + \sqrt{1 - \bar{\alpha}_t} \epsilon, \quad \epsilon \sim \mathcal{N}(0, I). \quad (2)$$

The generative task is to learn the reverse process  $p_\theta(x_{t-1}|x_t)$  such that a sample from  $x_T \sim \mathcal{N}(0, I)$  can be gradually denoised to yield  $x_0 \sim p_{\text{data}}$ . In practice, this reverse transition is parameterized by a neural network  $\epsilon_\theta(x_t, t)$  that predicts the noise, leading to

$$p_\theta(x_{t-1}|x_t) := \mathcal{N}\left(x_{t-1}; \frac{1}{\sqrt{\alpha_t}} \left(x_t - \frac{\beta_t}{\sqrt{1 - \bar{\alpha}_t}} \epsilon_\theta(x_t, t)\right), \sigma_t^2 I\right), \quad (3)$$

where  $\sigma_t^2$  can be fixed or learned. Training is performed with the denoising objective

$$\mathcal{L}_{\text{denoise}}(\theta) = \mathbb{E}_{x_0, \epsilon, t} [\|\epsilon - \epsilon_\theta(x_t, t)\|_2^2], \quad (4)$$

which corresponds to score matching [16], since  $\epsilon_\theta(x_t, t)$  approximates the score function  $-\sigma_t \nabla_{x_t} \log p(x_t)$ . Moreover, by reparameterization one can directly obtain an estimate of the clean sample  $x_0$  at timestep  $t$  as

$$\hat{x}_0(x_t) = \frac{1}{\sqrt{\bar{\alpha}_t}} \left(x_t - \sqrt{1 - \bar{\alpha}_t} \epsilon_\theta(x_t, t)\right), \quad (5)$$

which provides an explicit reconstruction of the data from noisy inputs and plays a key role in both DDPM sampling and extensions such as DDIM.

**Denoising diffusion implicit models.** Denoising Diffusion Implicit Models (DDIM) [42] build upon DDPM but modify the formulation to allow for a deterministic, non-Markovian sampling procedure that substantially accelerates generation. Instead of requiring  $T$  iterative reverse steps, DDIM introduces a reparameterized reverse process where the current latent  $x_t$  can be deterministically mapped to  $x_{t-1}$  using both the predicted clean image  $\hat{x}_0(x_t)$  and the predicted noise  $\epsilon_\theta(x_t, t)$ . Specifically, the reverse update is

$$x_{t-1} = \sqrt{\bar{\alpha}_{t-1}} \hat{x}_0(x_t) + \sqrt{1 - \bar{\alpha}_{t-1}} \epsilon_\theta(x_t, t). \quad (6)$$

This deterministic formulation allows skipping intermediate steps in the reverse trajectory without retraining the model, leading to fast sampling while preserving high generative quality. DDIM thus serves as a practical alternative to DDPM and is widely adopted in applications where efficient and scalable generation is crucial.

### B. Details of the multi-view diffusion model

**Implementation.** Our baseline model is CAT3D [12], a multi-view extension of Stable Diffusion 2.1 [38]. CAT3D adapts the latent text-to-image diffusion framework by inflating the 2D self-attention layers into 3D self-attention, enabling interactions across different views. Although the official implementation and model weights of CAT3D are not publicly available, we adopt the reproduction provided by MVGenMaster [6], which faithfully replicates CAT3D’s training and evaluation pipeline.

**Network architecture.** The underlying architecture consists of three downsampling blocks, one mid-block, and three upsampling blocks. Each downsampling block contains two layers, the mid-block contains one layer, and each upsampling block contains three layers. Each layer comprises a spatial convolution followed by a self-attention module.

In CAT3D, standard self-attention layers are replaced with inflated 3D self-attention layers to capture inter-view dependencies. This 3D attention is applied in all blocks except the first and last (*i.e.*, it is implemented in downsampling blocks 2 & 3, the mid-block, and upsampling blocks 1 & 2). In total, there are 11 inflated 3D self-attention layers used in our analysis.

The input images of resolution  $512 \times 512$  are encoded by the VAE encoder into latent features of size  $64 \times 64$ . Gaussian noise is added to the target latents for generation, while the reference latents remain unchanged. To form the conditioning latent, we first compute the Plücker ray embedding [52], which encodes per-pixel camera rays, and concatenate it with a binary visibility mask indicating the

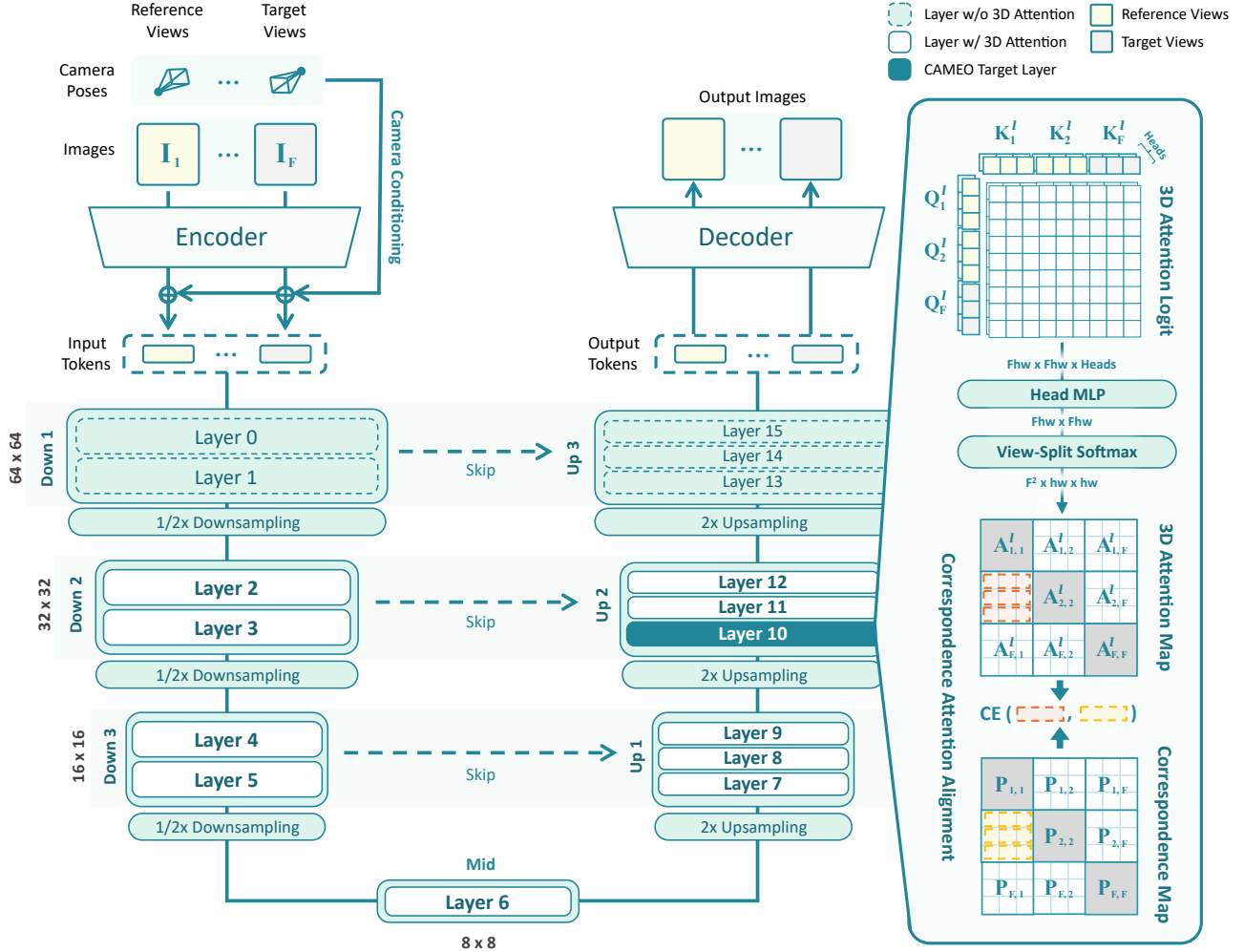


Figure 8. **Model architecture of CAT3D [12] with our proposed CAMEO framework.** While maintaining the original architecture, CAMEO introduces an additional correspondence-attention alignment loss,  $L_{\text{CAMEO}}$ , at the target layer (Layer 10) to supervise the attention map. Note that the visibility mask  $M_{i,j}$ , which filters out occluded or unreliable correspondences via 3D cycle consistency, is omitted in this visualization for simplicity.

reference images. This conditioning signal is then passed through a shallow convolutional network to match the dimensionality of the image latents. Finally, the conditioning latents are added to the image latents, producing the multi-view input representation for the diffusion U-Net.

Each downsampling block reduces the spatial resolution by a factor of 2, producing feature maps of size  $32 \times 32$ ,  $16 \times 16$ , and  $8 \times 8$ , respectively. The mid-block operates at the lowest resolution of  $8 \times 8$ . The upsampling blocks then progressively restore the spatial resolution back to  $16 \times 16$ ,  $32 \times 32$ , and  $64 \times 64$ . Finally, the latent is passed through the VAE decoder to reconstruct the full-resolution image of size  $512 \times 512$ .

## C. Detailed analysis

In Sec. 3.2, we report the attention analysis for layer  $l = 2, 4, 6, 7, 10$ , which are the first layers of each block. In Sec. C.1, we provide the qualitative analysis for all attention layers  $l = 2 - 12$ . In Sec. C.2, we provide details of the correspondence precision measured in the NAVI dataset [17] and report the precision for all attention layers. In Sec. C.3, we conduct a fine-grained analysis of layer-wise geometric correspondence in the diffusion transformer [26] based multi-view diffusion model to validate the generalizability of our systematic layer selection protocol.

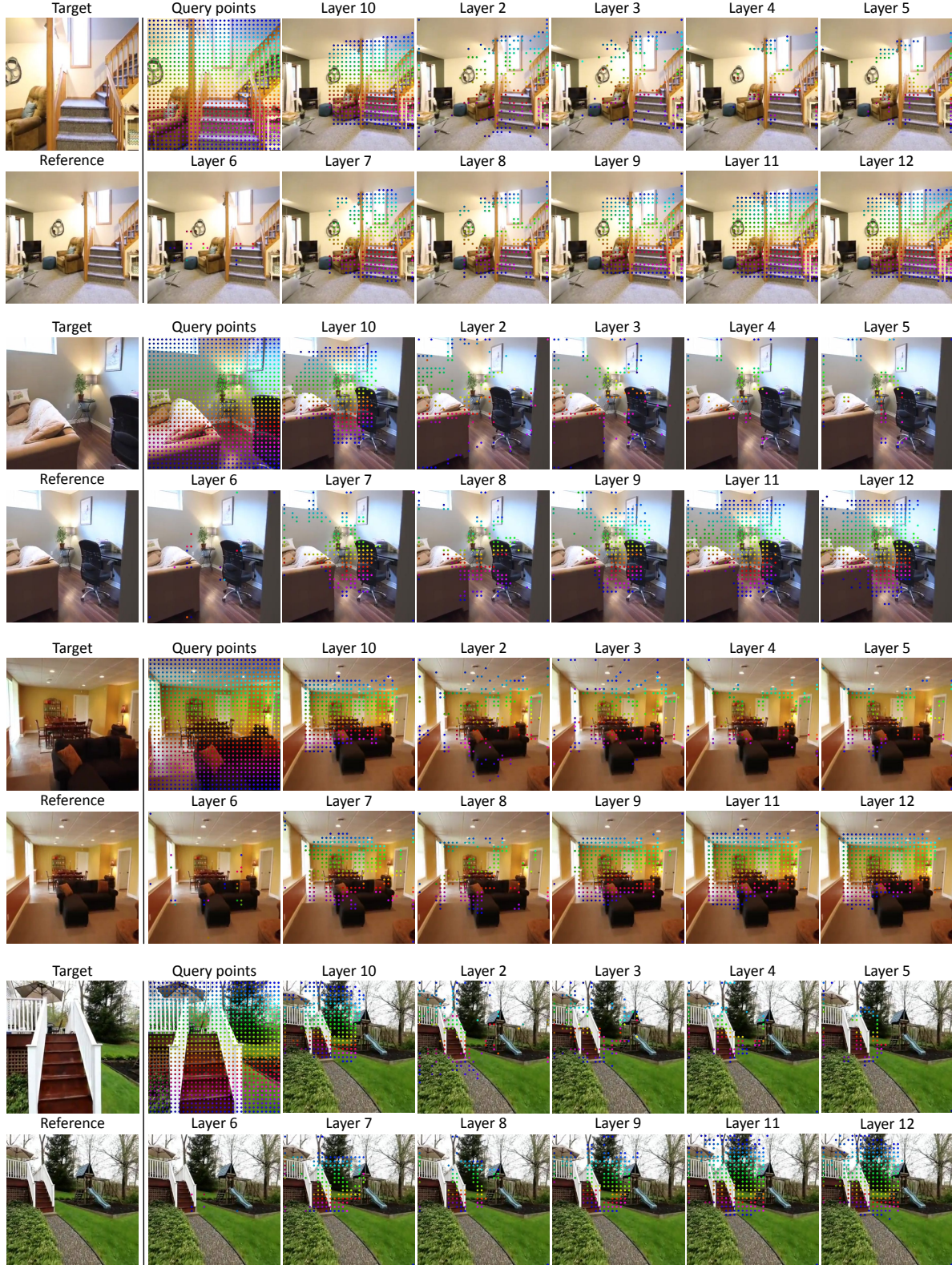


Figure 9. **Layer-wise behavior of the multi-view diffusion model (CAT3D [12])’s attention map.** For each query point on the target image, model’s maximum attending point in the reference image is marked with the same color as the query point.

## C.1. Qualitative analysis

**Layer-wise behavior.** As shown in Fig. 9, the attention map in layer  $l = 10$  of CAT3D [12] consistently attends to geometrically corresponding points relative to the query points. Similarly, layer  $l = 11, 12$  also attend to geometrically corresponding points, while earlier layers ( $l = 2 - 6$ ) do not. Layers  $l = 7 - 9$  exhibit similar behavior, but their corresponding points are sparse and noisy compared to those in deeper layers ( $l = 10, 12$ ). This layer-wise behavior demonstrates that attention maps in certain layers learn to capture geometric correspondence.

**Perturbation analysis.** Following [1, 21], we perturb the 3D self-attention maps of CAT3D [12] by enforcing the map into an identity mapping, where each query token attends exclusively to itself. The generation results in Fig. 10 demonstrate that perturbing layer  $l = 10$  causes severe structural fragmentation. In contrast, perturbing deeper layers ( $l = 11, 12$ ) results in color distortion or degradation but preserves the structural layout (*e.g.*, the tables and plaque remain recognizable). Notably, perturbing other layers has a negligible impact on the generated images. This implies that the geometric correspondence captured specifically at layer  $l = 10$  is fundamental to maintaining the structural consistency of the generated view.

## C.2. Correspondence estimation

**Dataset.** We evaluate geometric correspondence on the NAVI Dataset [17], which consists of 36 object scans with the ground-truth 3D geometry. The dataset provides high-quality assets, including intrinsics, extrinsics, depth maps, and object masks, enabling the inference of dense pixel-level correspondences. While Probe3D [11] utilized the *wild* split (same object, different backgrounds) of the dataset, we employ the *multiview* split to align with the Novel View Synthesis (NVS) setting, where the background remains consistent across views. To construct the evaluation set, we subsample 25% of the object views and select image pairs where the relative rotation  $\theta$  of the destination view is within  $120^\circ$ . This results in a total of 245 source-destination pairs.

**Procedure.** Given two images  $\mathbf{I}_1$  and  $\mathbf{I}_2$  of the same scene, we aim to identify pixel pairs corresponding to the same 3D surface point. We first extract a grid of feature descriptors from each image using the corresponding backbone, and resize this grid to a spatial resolution of  $128 \times 128$ . Correspondences are then estimated by matching all feature descriptors from  $\mathbf{I}_1$  to its nearest neighbor in  $\mathbf{I}_2$  based on a pre-defined distance function. To mitigate inaccurate matches, we apply Lowe’s ratio test [30], filtering for unique matches by comparing the distances to the first and second nearest neighbors. For each feature token  $p$ , let

$q_0$  and  $q_1$  be the first and second nearest neighbors, respectively. We compute the ratio  $r$  as

$$r = 1 - \frac{D(p, q_0)}{D(p, q_1)}, \quad (7)$$

where  $D(x, y)$  denotes the distance between two features: cosine distance for feature-based descriptors, and  $\ell_2$  distance in the 3D coordinate space for pointmap representations. We retain the top 1000 matches with the highest ratio  $r$  for evaluation.

**Evaluation.** We evaluate correspondence precision using the 3D Euclidean distance between the reprojected points. Given a correspondence pair, we back-project both image points into a common 3D space using ground-truth depth and camera parameters. A match is deemed correct if the 3D distance between the two points is below a threshold of  $\rho = 2\text{cm}$ . Note that we denote this metric as *Precision* instead of *Recall* (as used in Probe3D [11]) to accurately reflect our protocol of evaluating a fixed number of top-1,000 candidates.

In Fig. 5b, we report the per-bin Precision@2cm averaged over samples in each angular bin. In the following section, we provide the detailed setup for correspondence extraction in CAT3D [12], SD2.1 [38], DINOV3 [41], and VGGT pointmap [48], Dense SIFT [27].

- **CAT3D.** For the analysis, we evaluate CAT3D [12] trained on the object-centric dataset CO3D [37]. We consider  $\mathbf{I}_1$  and  $\mathbf{I}_2$  as target and reference views. And we perform inference without camera conditioning and extract correspondences in a noise-free setting, *i.e.*, without injecting additional diffusion noise. Query  $\mathbf{Q}_1^l$  and key  $\mathbf{K}_2^l$  descriptors are extracted at each layer  $l$  ( $32 \times 32$  to  $8 \times 8$  resolution).
- **SD2.1.** We aim to analyze the correspondence in the attention map before finetuning. Therefore, using CAT3D [12] architecture, we initialize the model weights with SD2.1 and measure the correspondence in the attention map.
- **DINOV3.** DINOV3 [41] is a state-of-the-art visual foundation model used across many downstream tasks, such as image retrieval, semantic segmentation, and dense matching. It is known for producing reliable patch-level matches. We extract patch embeddings on a  $32 \times 32$  grid and compute cosine similarity between patches across views to identify correspondences. We report the results for both ViT-B/16 and ViT-L/16 variants in Tab. 8.
- **VGGT pointmap.** We measure geometric correspondence based on  $\ell_2$ -norm nearest neighbor search. Since the pointmap explicitly encodes 3D coordinates at a resolution of  $518 \times 518$ , we use distance-based matching rather than cosine similarity.

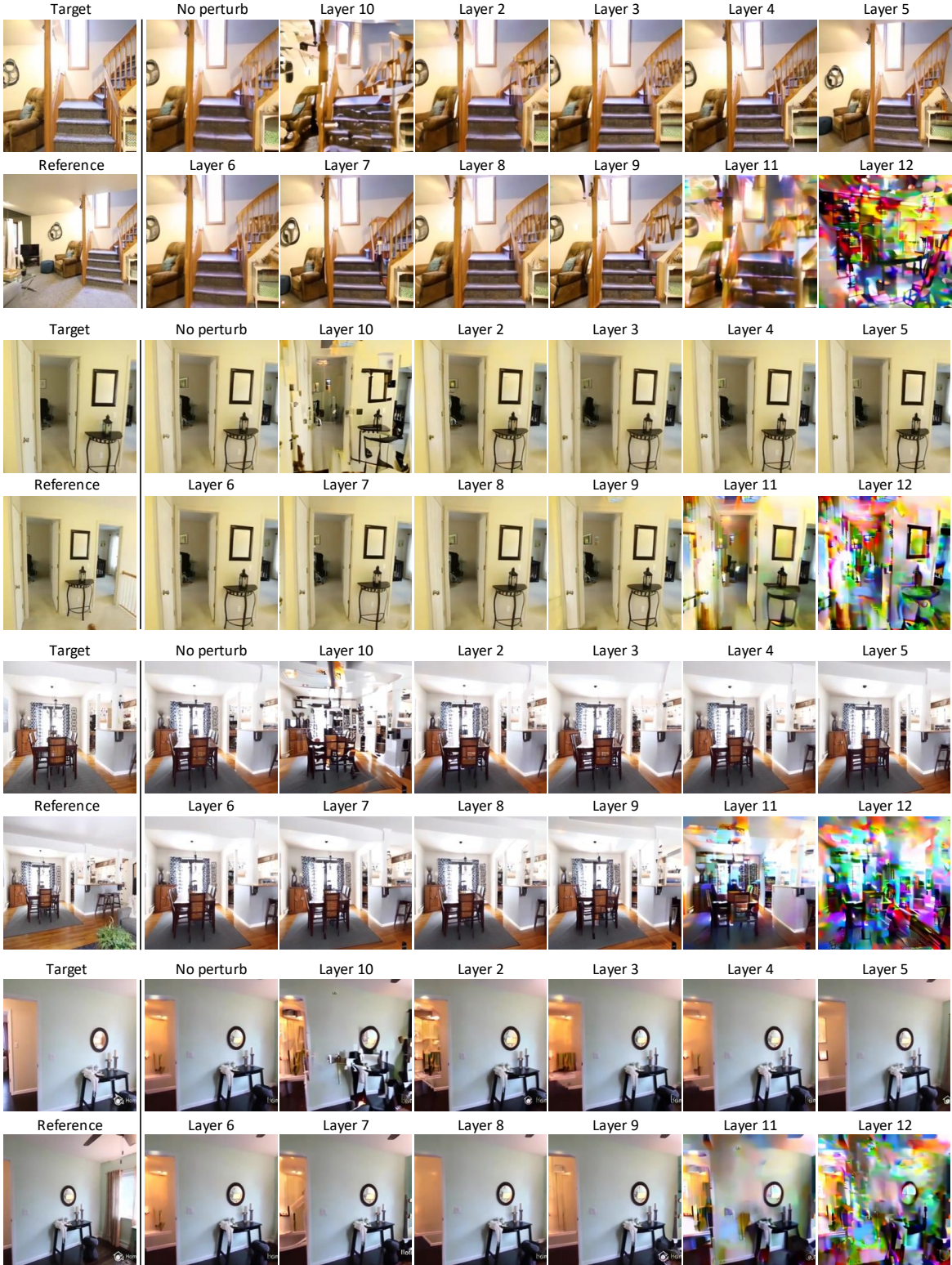


Figure 10. **Layer-wise perturbation results.** Perturbing earlier layers barely changes generation quality, while perturbing layer 10 collapses geometric consistency and severely degrades quality.

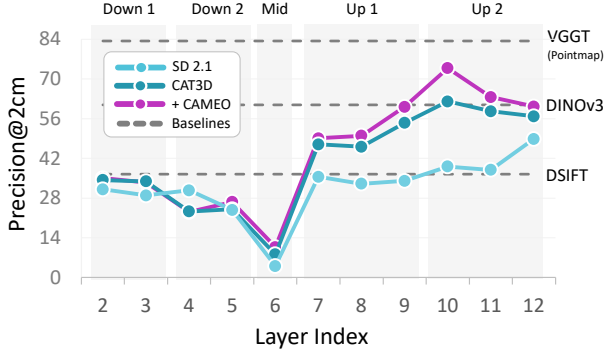


Figure 11. Analysis of geometric correspondence in all attention layers of the multi-view diffusion model [12]. Correspondence precision across all attention layers ( $l = 2 - 12$ ), with other baselines [27, 38, 41, 48].

- **Dense SIFT.** For Dense SIFT, we follow the SIFT Flow [27] pipeline and compute dense SIFT descriptors on a multi-scale pyramid. We aggregate the descriptors onto a  $128 \times 128$  grid and apply normalization following RootSIFT [3]. The resulting descriptors are used as feature tokens for cosine-distance matching, as in the other methods.

**Correspondence precision.** In Fig. 11, we present layer-wise correspondence precision across the U-Net architecture, with detailed quantitative results in Tab. 8. In the downsampling blocks ( $l = 2 - 5$ ), SD2.1 [38] and CAT3D [12] exhibit comparable performance, both showing a sharp decline at the bottleneck ( $l = 6$ ) due to spatial compression. A clear divergence emerges in the upsampling blocks ( $l = 7 - 12$ ), where CAMEO demonstrates improved consistency over SD2.1 [38]. Among all layers,  $l = 10$  shows the strongest correspondence, validating our analysis in Sec. 3.2 that  $l = 10$  encodes the geometric correspondence.

With alignment, CAMEO consistently achieves higher correspondence precision than CAT3D [12] across the upsampling blocks. Notably, even though our supervision is applied solely to the single target layer ( $l = 10$ ), performance gains are observed throughout the neighboring upsampling layers ( $l = 7 - 12$ ). This demonstrates that aligning one layer is sufficient to guide the model toward learning precise correspondences.

### C.3. Generalizability of layer selection

In Sec. 4, we demonstrate the generalizability of CAMEO by applying it to the diffusion transformer (DiT) architecture [26]. In this section, we provide a fine-grained analysis of the layer-wise geometric correspondence in the DiT-based multi-view diffusion model to investigate the generalizability of systematic layer selection. Following the evaluation protocol in Sec. 3.2, we measure the geometric correspondence precision across all layers of the DiT model.

As detailed in Tab. 9, we observe that layer  $l = 32$  exhibits the highest precision.

The layer-wise behavior of the DiT-based model differs from that of the UNet-based model [12] due to their architectural differences. For instance, deeper layers ( $l = 35 - 39$ ) show low precision in geometric correspondence. However, despite these differences, the DiT-based model still captures geometric correspondence in specific layers, and CAMEO improves model performance by supervising it with our simple attention alignment method, as shown in Tab. 5. These results demonstrate that CAMEO can be generalized to multi-view diffusion models with diverse architectures. Furthermore, our key finding—that multi-view diffusion models progressively learn to capture geometric correspondence in their attention maps during training—holds across different architectural designs.

## D. Implementation details

In Sec. D.1, we provide the evaluation settings. In Sec. D.2, we explain the detailed method to obtain correspondences from pointmaps, then evaluate the accuracy and efficiency. In Sec. D.3, we provide implementation details of a DiT-based [26] and a state-of-the-art multi-view diffusion model [6].

### D.1. Evaluation settings

In Sec. 4.2, we evaluate CAMEO against baselines [12, 54] on the RealEstate10K [56], CO3D [37], and DTU [18] datasets. In the evaluation, to assess the model’s robustness in maintaining view consistency under challenging scenarios, we curate a hard evaluation set. Specifically, for RealEstate10K [56] and CO3D [37], we sample images that exhibit large viewpoint changes. While this aggressive sampling strategy naturally yields lower quantitative scores across all evaluated models (as seen in Tab. 1), it is essential for identifying failure cases in geometric consistency and rigorously assessing robustness under challenging scenarios.

### D.2. Correspondence from pointmap

**Method.** DUST3R [49] introduces an algorithm to establish pixel correspondences between two images through nearest neighbor search in 3D pointmap space. Specifically, for an image  $\mathbf{I}_i \in \mathbb{R}^{H \times W \times 3}$ , a pointmap  $\mathbf{X}_i \in \mathbb{R}^{H \times W \times 3}$  represents the 3D coordinates of each pixel. Given an image pair  $(\mathbf{I}_i, \mathbf{I}_j)$  where  $i \neq j$ , correspondences are established by computing mutual nearest neighbors between pixel locations  $\mathbf{y}_i$  and  $\mathbf{y}_j$ :

$$\{(\mathbf{y}_i, \mathbf{y}_j) \mid \mathbf{y}_j = \text{NN}^{i,j}(\mathbf{y}_i) \text{ and } \mathbf{y}_i = \text{NN}^{j,i}(\mathbf{y}_j)\}, \quad (8)$$

where  $\text{NN}^{i,j}(\mathbf{y}_i) := \arg \min_{k \in \{1, \dots, HW\}} \|\mathbf{X}_i(\mathbf{y}_i) - \mathbf{X}_j(k)\|_2$  denotes the nearest neighbor of pixel  $\mathbf{y}_i$  in view  $j$  within 3D

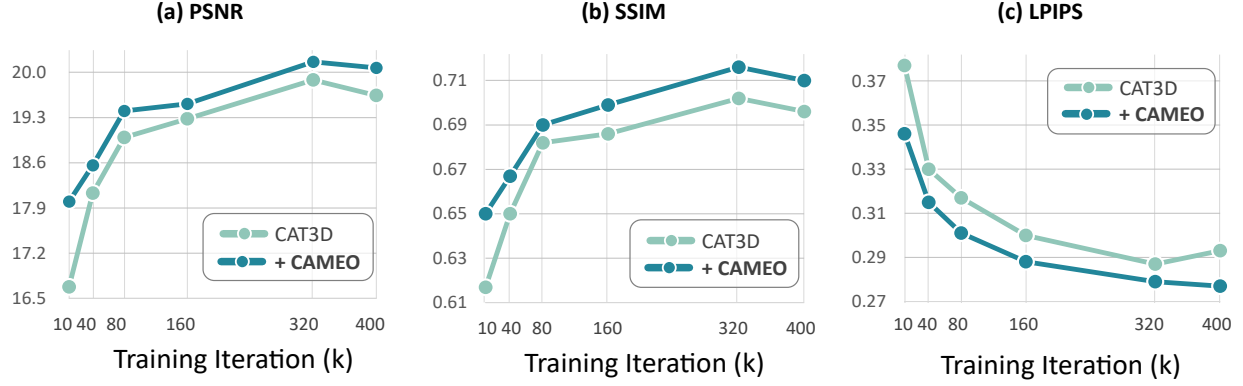


Figure 12. The relative improvements of CAMEO over CAT3D [12] on RealEstate10K [56] dataset.

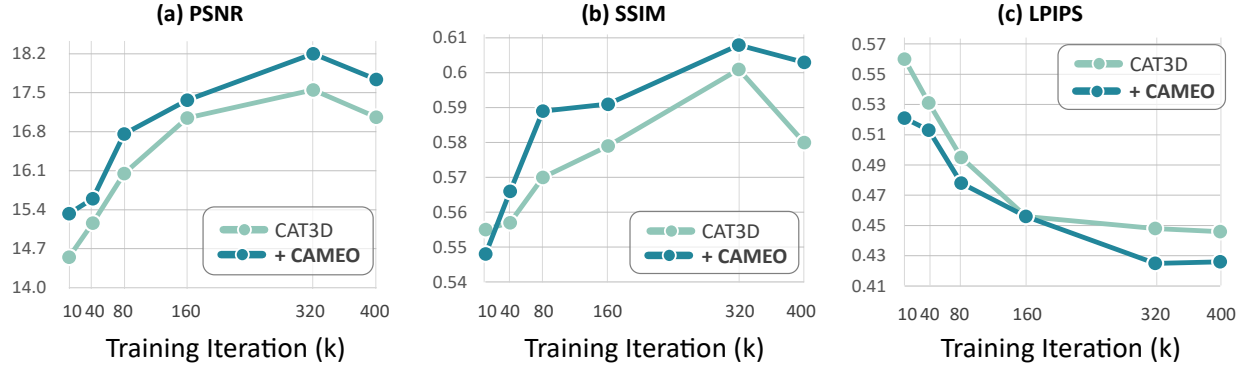


Figure 13. The relative improvements of CAMEO over CAT3D [12] on CO3D [37] dataset.

space. We extend this algorithm to token-level resolution by downsampling the pointmaps, and introduce a cycle consistency threshold  $\tau$  to replace the exact mutual matching criterion.

**Accuracy.** We employ VGGT [48] to obtain pointmaps, as it reports superior performance compared to previous geometry prediction models, such as DUS3R [49] and MAST3R [23]. As illustrated in Fig. 5a, VGGT pointmaps achieve the correspondence precision of 83.32, significantly outperforming DINOv2 at 60.84 and Dense SIFT [27] at 36.43.

Table 6. Runtime and peak GPU memory usage across different numbers of input frames. Runtime is measured in seconds, and GPU memory usage is reported in gigabytes.

Input Frames		1	2	4	8	10	20	50
Time (s)	Pointmaps	0.13	0.16	0.27	0.52	0.68	1.73	5.46
	Tracking	1.44	2.95	6.30	14.10	18.91	53.10	304.58

Mem. (GB)		2.1	2.4	3.1	4.5	5.3	8.8	19.5
Pointmaps	Tracking	2.3	2.7	3.4	5.0	5.7	9.6	21.1

**Efficiency.** VGGT [48] employs a simple feed-forward approach that build pointmaps in only 0.2 seconds. Although tracking is an alternative method for producing dense correspondences between images, dense tracking is computationally prohibitive. Moreover, tracking requires  $F$  separate inferences to supervise the 3D self-attention map, where  $F$  is the total number of views. We evaluate inference runtime and peak GPU memory for obtaining pointmaps and tracks from VGGT [48] with varying numbers of input frames. Measurements are conducted using a single NVIDIA A6000 GPU with images at  $336 \times 518$  resolution. For tracking, we use 1024 query points, equivalent to the total number of query tokens in the attention map at layer  $l = 10$  of CAT3D [12]. As shown in Tab. 6, pointmap inference is significantly faster and more memory-efficient than tracking.

### D.3. Other architectures

**State-of-the-art multi-view diffusion model.** We implement MVGenMaster [6] based on the officially released code. We use an off-the-shelf geometry model [48] to obtain depth maps for geometric conditions. We initialize the

model with Stable Diffusion 2.1 [38] weights, and train the model on the RealEstate10K [56] dataset with a batch size of 3. Other training and evaluation details are identical to those in the main model experiment.

**DiT-based multi-view diffusion model.** Following Matrix3D [31], we implement a multi-view diffusion model based on a pre-trained text-to-image diffusion transformer (DiT) [26]. However, instead of using an external transformer encoder to embed conditional inputs as in Matrix3D [31], we adopt a simpler approach by inflating the self-attention to 3D self-attention, similar to our baseline [12]. Specifically, we concatenate the query, key, and value matrices of each self-attention layer, and omit the cross-attention layer and text encoder. Following Matrix3D [31], we employ Rotary Positional Embedding (RoPE) [43] to encode each token’s position and absolute sinusoidal positional encoding [10] to encode the viewpoint index. We use Plücker rays to represent camera poses and add the camera pose embeddings as residuals. The model is initialized with Hunyuan-DiT [26] weights and trained on the RealEstate10K [56] dataset with a batch size of 4. All other training and evaluation details remain identical to those of the main model.

## E. Ablation studies

Table 7. **Ablation study for supervision target.** Evaluated on RealEstate10K [56] at 40k iterations.

Supervision Targets	PSNR↑	SSIM↑	LPIPS↓
Feature Cost	18.17	0.650	0.333
Attention	<b>18.42</b>	<b>0.662</b>	<b>0.323</b>

Motivated by DIFT [46], which demonstrates that intermediate features from Stable Diffusion 2.1 [38] encode correspondence, we investigate the impact of the supervision target. Specifically, we compare two approaches at layer  $l = 10$ : (1) supervising the feature similarity map derived from the layer’s output features, and (2) directly supervising the attention map. We train the models with a batch size 6, while other training and evaluation settings remain identical to the ablation experiments. Tab. 7 shows that supervising the attention map yields superior performance. This confirms that geometric correspondence is most effectively regulated directly within the attention mechanism, whereas feature similarity requires computing an additional cost map extraneous to the original architecture.

## F. Qualitative results

We provide additional qualitative comparisons of CAMEO on both scene-level [56] and object-centric [18, 37] set-

tings. We present qualitative comparisons against the baseline, highlighting improved geometric consistency. Figs. 15 to 17 shows qualitative examples organized by training iteration. We also provide the qualitative results of CAMEO on the state-of-the-art model [6] and DiT-based [26] model in Fig. 18 and Fig. 19.

## G. 3D reconstruction

Following CAT3D [20], we also perform 3D reconstruction using the novel views generated by the model. We create camera trajectories to generate novel view images and use them to optimize 3DGS [20]. Specifically, we first run the multi-view diffusion models on 2-view settings, where the first and the last cameras are input views, and sample target camera trajectories between them evenly. The total number of views are 100 (2 input views and 98 generated views). We then optimize 3DGS with  $\ell_1$ , SSIM loss, alongside LPIPS loss following CAT3D [12], to reconstruct 3D scenes from generated novel views.

We provide the 3D reconstruction results on DTU [18] dataset in Fig. 14. While CAT3D [12] fails to reconstruct 3D scenes, CAMEO can faithfully reconstruct scenes through 3DGS. This demonstrates that CAMEO produces view-consistent images, leading to higher-quality 3D reconstructions than the baseline [12].

## H. Limitations

Our method may struggle with extreme viewpoint changes where reference and target views share minimal or no visual overlap. In such scenarios, establishing cross-view correspondence becomes inherently infeasible. Since CAMEO is designed to leverage geometric correspondences between views, its effectiveness is naturally constrained under extreme viewpoint gaps. This reflects a fundamental challenge in novel view synthesis. To address such scenarios, alternative strategies can be employed, sequentially generating intermediate views with each step conditioned on previously generated images [25, 47].

## I. Future work

- **Beyond novel view synthesis.** Our method targets multi-view diffusion for novel view synthesis. Extending correspondence-aware supervision to video diffusion, 4D reconstruction, or other multi-modal tasks remains an open direction.
- **Semantic correspondences.** We demonstrate that specific layers encode geometric correspondence and improve performance through geometric alignment. As an extension, semantic correspondence may be encoded in other layers, and leveraging this signal could further enhance generation quality and semantic understanding.



Figure 14. **3D reconstruction results.** We input 2 views and generate novel views to optimize 3DGS [20]. In the 3DGS rendering results, CAMEO exhibits consistent rendered images while CAT3D [12] fails.

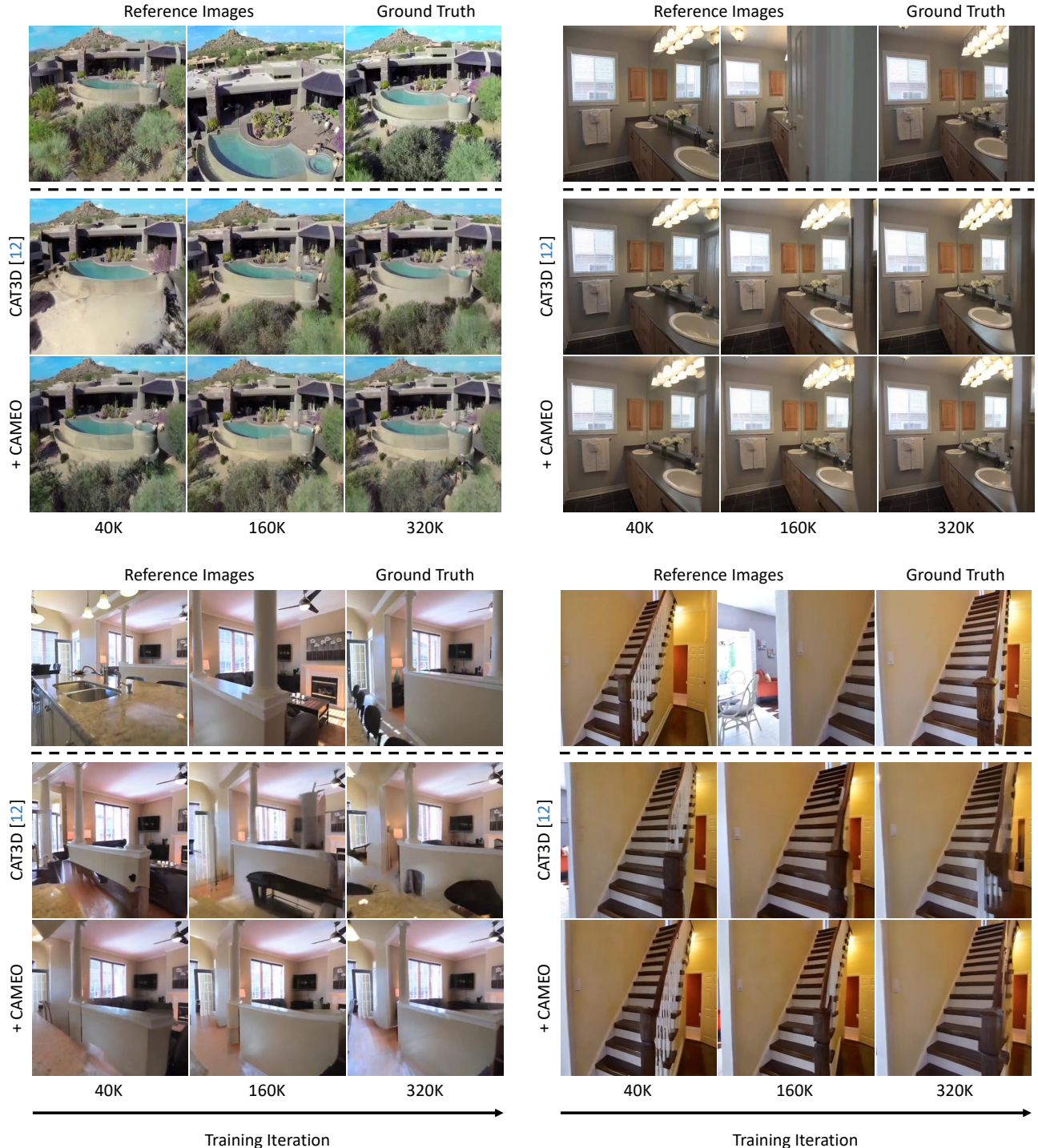


Figure 15. **Qualitative results** on RealEstate10K [56]. CAMEO improves learning efficiency while significantly enhancing geometric consistency compared to the baseline, as explicit correspondence supervision encourages faster convergence in novel view synthesis.

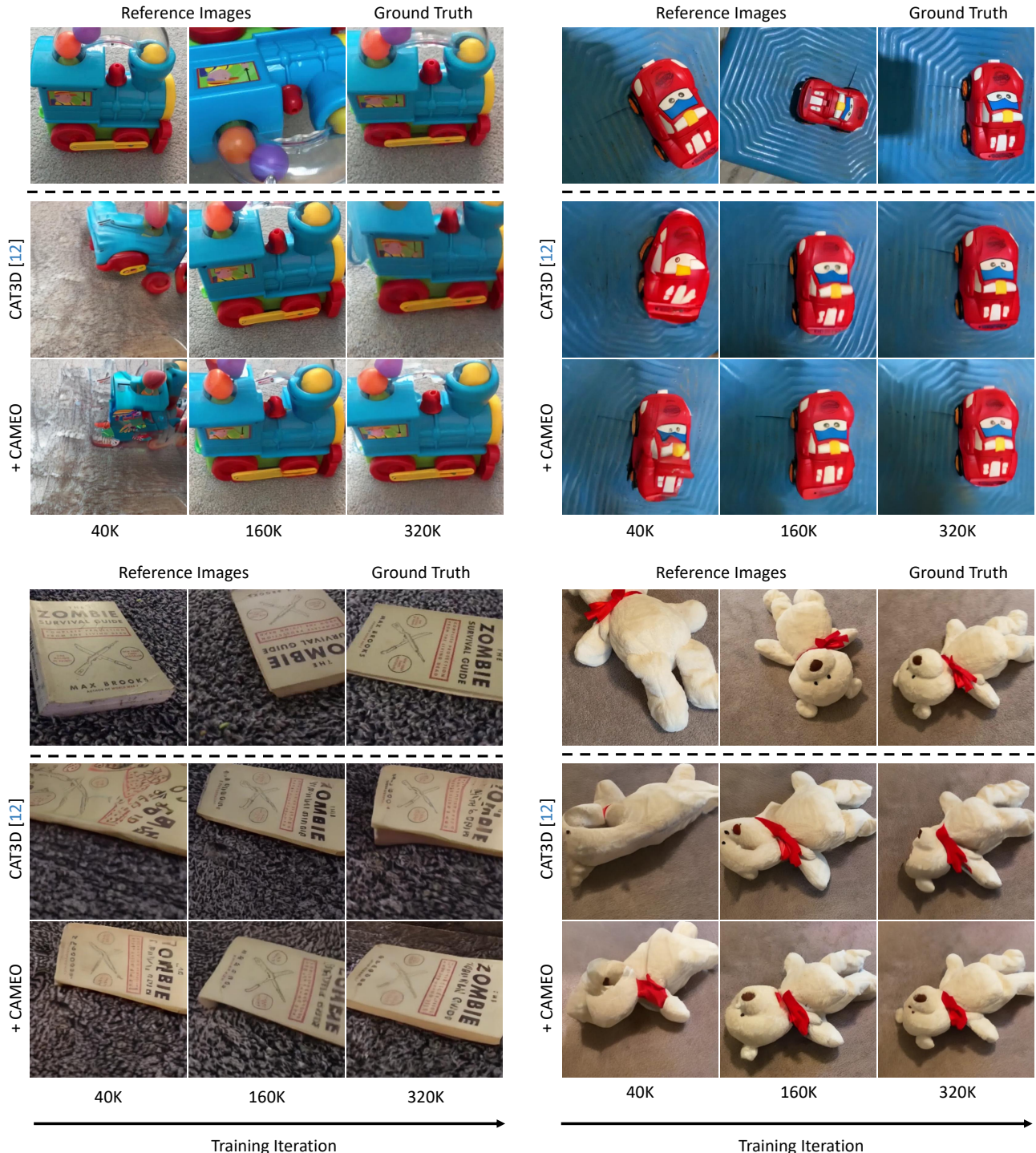


Figure 16. **Qualitative results on CO3D [37].** CAMEO improves learning efficiency while significantly enhancing geometric consistency compared to the baseline, as explicit correspondence supervision encourages faster convergence in novel view synthesis.

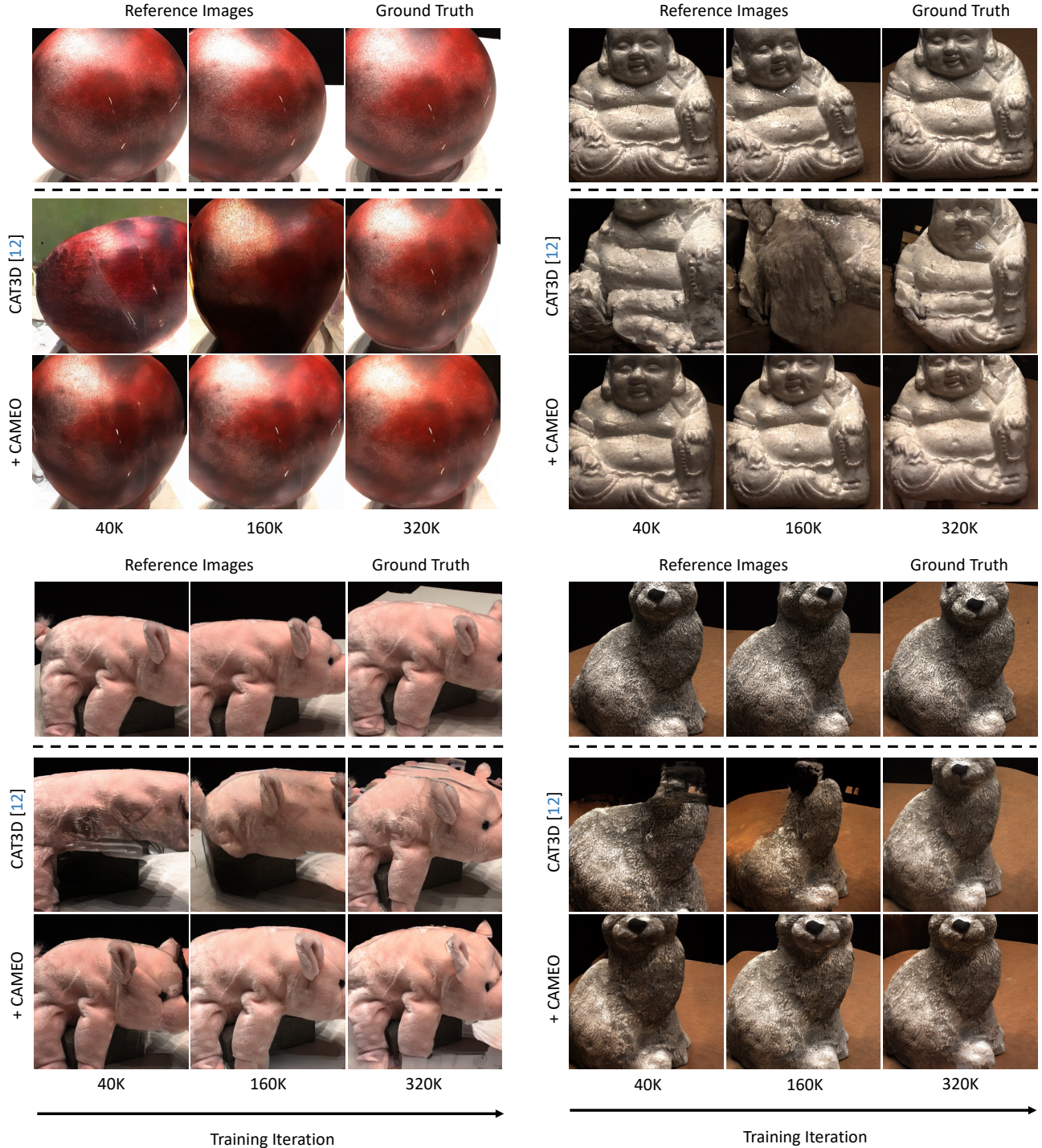


Figure 17. **Qualitative results on DTU [18] (Out-of-domain).** CAMEO improves learning efficiency while significantly enhancing geometric consistency compared to the baseline, as explicit correspondence supervision encourages faster convergence in novel view synthesis.

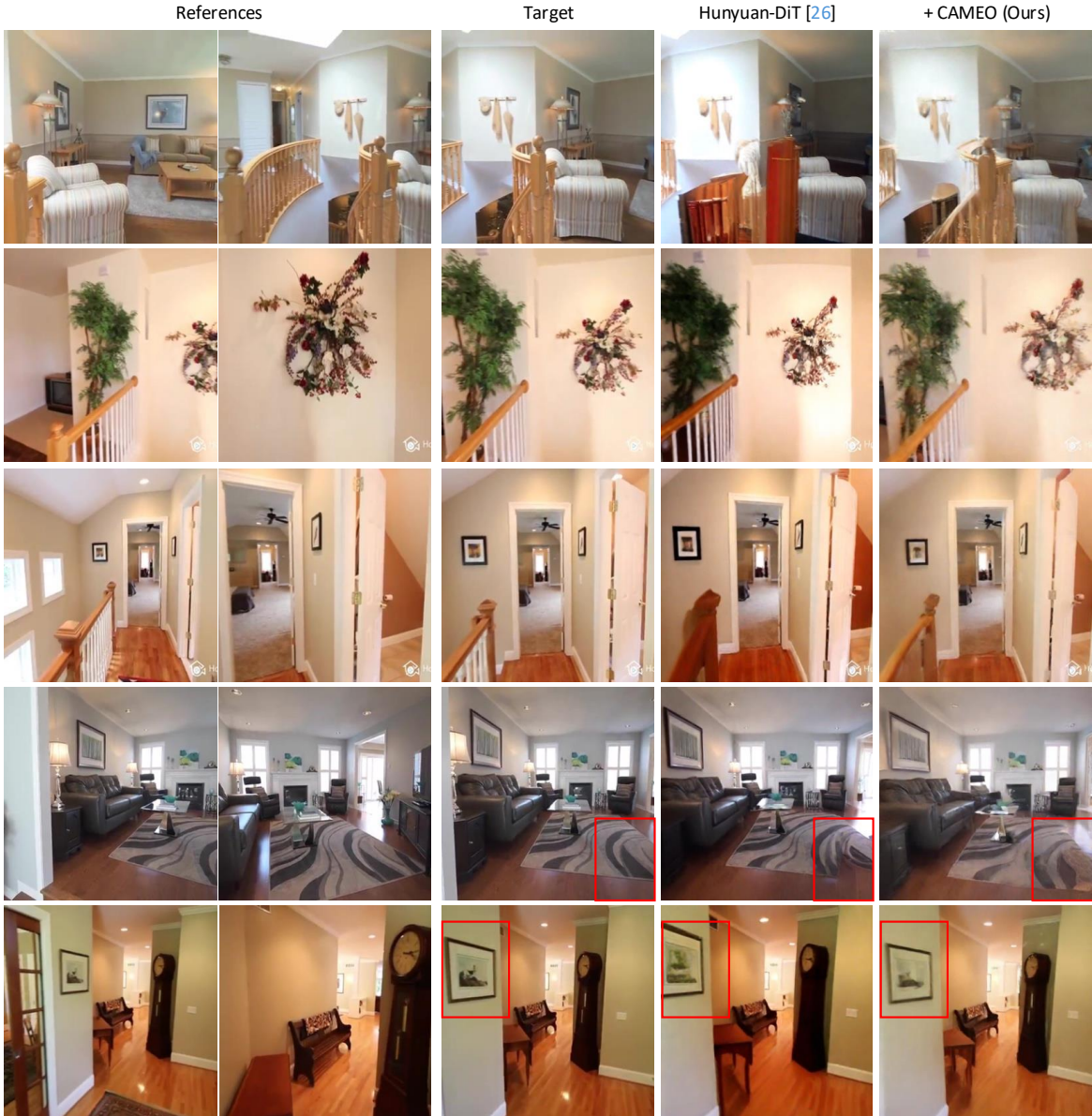


Figure 18. **Qualitative results of DiT-based model [26] on RealEstate10K [56].** CAMEO enhances geometric consistency compared to the baseline. By incorporating explicit correspondence supervision, our method encourages the model to learn and preserve accurate structural relationships across views.

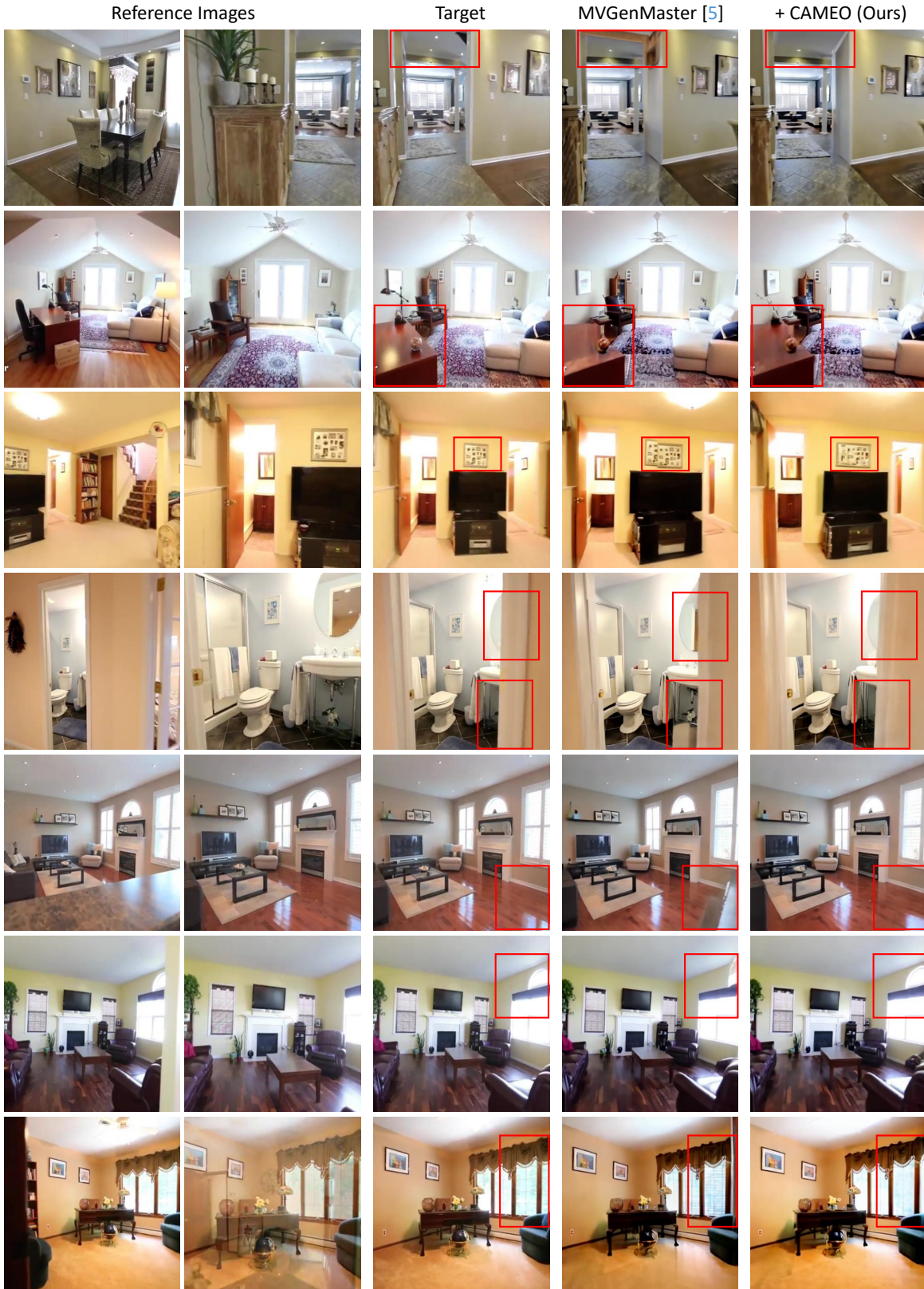


Figure 19. **Qualitative results of MVGenMaster on RealEstate10K [56].** CAMEO enhances geometric consistency compared to the baseline. By incorporating explicit correspondence supervision, our method encourages the model to learn and preserve accurate structural relationships across views.

Table 8. **Performance comparison on the NAVI [17] dataset.** We report Precision@2cm following the Probe3d [11] protocol. Best results per category are marked in **bold**. CAT3D [12] and CAMEO are trained on the Co3D [37] dataset for 320k training iterations.

Model	Feature Grid	Precision@2cm				
		Overall	0 – 30°	30 – 60°	60 – 90°	90 – 120°
VGGT Pointmaps [48]	518 × 518	<b>83.32</b>	<b>97.41</b>	<b>92.28</b>	<b>83.12</b>	<b>63.86</b>
Dense SIFT [27]	128 × 128	36.43	90.02	53.82	14.51	8.68
DINOv3 [41]	ViT-L/16	32 × 32	<b>60.84</b>	<b>95.66</b>	<b>78.36</b>	<b>50.51</b>
	ViT-B/16	32 × 32	56.68	94.34	74.91	44.05
SD2.1 [38]	2	32 × 32	31.09	52.88	39.32	23.07
	3		28.94	45.68	36.17	21.97
	4	16 × 16	30.75	57.41	39.66	22.46
	5		23.81	37.77	31.97	18.59
	6	8 × 8	4.05	1.67	4.36	5.70
	7	16 × 16	35.47	72.65	49.14	21.94
	8		33.04	71.89	45.55	19.48
	9		34.07	70.16	45.83	21.87
	10	32 × 32	39.12	84.87	56.98	21.52
	11		37.95	80.87	53.71	21.20
	12		<b>48.85</b>	<b>90.24</b>	<b>68.47</b>	<b>32.51</b>
CAT3D [12]	2	32 × 32	34.36	63.67	45.69	22.80
	3		33.90	62.19	44.60	23.31
	4	16 × 16	23.28	40.96	30.43	17.01
	5		24.06	41.87	32.70	18.08
	6	8 × 8	8.20	10.44	10.28	8.16
	7	16 × 16	46.95	76.76	61.23	39.89
	8		46.07	78.65	61.05	36.65
	9		54.50	84.96	69.48	45.64
	10	32 × 32	<b>62.07</b>	<b>94.33</b>	<b>79.63</b>	<b>53.73</b>
	11		58.61	92.41	77.70	48.06
	12		56.82	80.80	73.97	45.93
CAMEO	2	32 × 32	35.05	64.84	46.83	24.28
	3		33.53	59.32	44.21	24.29
	4	16 × 16	23.10	39.91	30.60	16.85
	5		26.61	45.17	35.18	20.82
	6	8 × 8	10.74	11.75	12.03	9.43
	7	16 × 16	49.08	81.05	64.56	41.74
	8		49.97	76.29	62.59	45.38
	9		60.19	86.81	71.84	55.57
	10	32 × 32	<b>73.80</b>	<b>94.88</b>	<b>84.80</b>	<b>72.92</b>
	11		63.62	93.23	79.89	57.12
	12		60.30	90.89	75.21	51.11

Table 9. Correspondence precision per layer on DiT-based multi-view diffusion model [26]. The best performing layer is in **bold**. The model is trained on the Co3D [37] dataset for 60k iterations.

Layer	Overall	Precision@2cm				Layer	Overall	Precision@2cm			
		0–30°	30–60°	60–90°	90–120°			0–30°	30–60°	60–90°	90–120°
0	11.35	19.27	13.47	8.57	7.31	20	28.60	72.90	38.19	14.18	7.54
1	27.90	72.63	36.92	13.46	7.37	21	26.01	65.27	34.99	13.41	6.51
2	27.78	72.68	37.53	12.64	7.02	22	30.19	71.07	41.21	15.83	9.16
3	28.05	71.42	37.53	13.76	7.51	23	41.06	87.01	56.14	26.42	12.22
4	32.80	78.74	45.02	16.11	10.03	24	27.31	58.13	37.45	16.50	9.06
5	30.19	73.00	40.27	15.92	9.16	25	26.83	67.62	36.38	13.32	6.77
6	30.98	73.98	41.08	16.62	9.96	26	43.62	83.37	56.45	32.05	17.69
7	31.21	75.50	42.26	16.06	9.12	27	30.24	74.41	39.71	16.56	8.53
8	31.93	75.68	41.74	17.75	10.62	28	24.84	67.21	31.61	12.25	6.41
9	30.31	74.68	40.34	15.55	9.03	29	48.14	90.51	64.27	34.97	18.28
10	35.78	80.02	47.87	20.74	12.24	30	35.91	86.29	48.98	19.81	8.84
11	31.90	78.01	43.12	16.28	9.10	31	33.55	82.89	45.26	17.64	8.61
12	30.84	76.69	41.19	15.89	8.52	32	<b>50.22</b>	<b>90.42</b>	<b>68.32</b>	<b>36.55</b>	<b>19.62</b>
13	33.96	73.14	45.01	20.81	12.49	33	28.21	73.34	38.03	13.35	6.91
14	28.05	64.74	37.32	14.80	8.87	34	41.41	85.19	56.78	26.22	14.06
15	23.99	55.96	33.05	12.66	7.09	35	31.79	74.43	42.44	17.53	10.13
16	23.53	49.95	31.75	15.05	7.58	36	34.93	76.04	48.45	20.60	10.53
17	26.96	61.90	34.44	16.67	9.21	37	29.22	72.24	37.82	15.89	8.91
18	26.09	64.89	34.61	13.30	7.70	38	30.10	73.30	41.63	15.26	7.64
19	26.92	67.35	35.95	13.30	7.87	39	25.94	69.89	34.34	11.83	6.25

## References

[1] Donghoon Ahn, Hyoungwon Cho, Jaewon Min, Wooseok Jang, Jungwoo Kim, SeonHwa Kim, Hyun Hee Park, Kyong Hwan Jin, and Seungryong Kim. Self-rectifying diffusion sampling with perturbed-attention guidance, 2025. 4, 5, 13

[2] Hongyu An, Jin Hyeon Kim, Seonghoon Park, Jaewoo Jung, Jisang Han, Sunghwan Hong, and Seungryong Kim. Cross-view completion models are zero-shot correspondence estimators. In *Proceedings of the Computer Vision and Pattern Recognition Conference*, pages 1103–1115, 2025. 4

[3] Relja Arandjelović and Andrew Zisserman. Three things everyone should know to improve object retrieval. In *2012 IEEE conference on computer vision and pattern recognition*, pages 2911–2918. IEEE, 2012. 15

[4] Andreas Blattmann, Tim Dockhorn, Sumith Kulal, Daniel Mendelevitch, Maciej Kilian, and Dominik Lorenz. Stable video diffusion: Scaling latent video diffusion models to large datasets. *arXiv preprint arXiv:2311.15127*, 2023. 2

[5] Tim Brooks, Aleksander Holynski, and Alexei A Efros. Instructpix2pix: Learning to follow image editing instructions. In *Proceedings of the IEEE/CVF conference on computer vision and pattern recognition*, pages 18392–18402, 2023. 3

[6] Chenjie Cao, Chaohui Yu, Shang Liu, Fan Wang, Xiangyang Xue, and Yanwei Fu. Mvgenmaster: Scaling multi-view generation from any image via 3d priors enhanced diffusion model. In *Proceedings of the Computer Vision and Pattern Recognition Conference*, pages 6045–6056, 2025. 1, 2, 3, 5, 6, 8, 9, 10, 15, 16, 17

[7] Hila Chefer, Yuval Alaluf, Yael Vinker, Lior Wolf, and Daniel Cohen-Or. Attend-and-excite: Attention-based semantic guidance for text-to-image diffusion models, 2023. 3

[8] Yuedong Chen, Haofei Xu, Chuanxia Zheng, Bohan Zhuang, Marc Pollefeys, Andreas Geiger, Tat-Jen Cham, and Jianfei Cai. Mvsplat: Efficient 3d gaussian splatting from sparse multi-view images. *arXiv preprint arXiv:2403.14627*, 2024. 6

[9] Prafulla Dhariwal and Alexander Nichol. Diffusion models beat gans on image synthesis. *Advances in neural information processing systems*, 34:8780–8794, 2021. 6

[10] Alexey Dosovitskiy. An image is worth 16x16 words: Transformers for image recognition at scale. *arXiv preprint arXiv:2010.11929*, 2020. 17

[11] Mohamed El Banani, Amit Raj, Kevis-Koktsi Maninis, Abhishek Kar, Yuanzhen Li, Michael Rubinstein, Deqing Sun, Leonidas Guibas, Justin Johnson, and Varun Jampani. Probing the 3d awareness of visual foundation models. In *Proceedings of the IEEE/CVF Conference on Computer Vision and Pattern Recognition*, pages 21795–21806, 2024. 4, 13, 24

[12] Ruiqi Gao, Aleksander Holynski, Philipp Henzler, Arthur Brussee, Ricardo Martin-Brualla, Pratul Srinivasan, Jonathan T Barron, and Ben Poole. Cat3d: Create anything in 3d with multi-view diffusion models. *arXiv preprint arXiv:2405.10314*, 2024. 1, 2, 3, 4, 5, 6, 7, 8, 9, 10, 11, 12, 13, 15, 16, 17, 18, 24

[13] Amir Hertz, Ron Mokady, Jay Tenenbaum, Kfir Aberman, Yael Pritch, and Daniel Cohen-Or. Prompt-to-prompt image editing with cross attention control. *arXiv preprint arXiv:2208.01626*, 2022. 3

[14] Jonathan Ho, Ajay Jain, and Pieter Abbeel. Denoising diffusion probabilistic models. *Advances in neural information processing systems*, 33:6840–6851, 2020. 2, 6, 10

[15] Sungwon Hwang, Hyojin Jang, Kinam Kim, Minho Park, and Jaegul Choo. Cross-frame representation alignment for fine-tuning video diffusion models. *arXiv preprint arXiv:2506.09229*, 2025. 3

[16] Aapo Hyvärinen and Peter Dayan. Estimation of non-normalized statistical models by score matching. *Journal of Machine Learning Research*, 6(4), 2005. 10

[17] Varun Jampani, Kevis-Koktsi Maninis, Andreas Engelhardt, Arjun Karpur, Karen Truong, Kyle Sargent, Stefan Popov, André Araujo, Ricardo Martin Brualla, Kaushal Patel, et al. Navi: Category-agnostic image collections with high-quality 3d shape and pose annotations. *Advances in Neural Information Processing Systems*, 36:76061–76084, 2023. 4, 11, 13, 24

[18] Rasmus Jensen, Anders Dahl, George Vogiatzis, Engil Tola, and Henrik Aanæs. Large scale multi-view stereopsis evaluation. In *2014 IEEE Conference on Computer Vision and Pattern Recognition*, pages 406–413. IEEE, 2014. 2, 6, 7, 8, 15, 17, 21

[19] Hyeonho Jeong, Chun-Hao P Huang, Jong Chul Ye, Niloy J Mitra, and Duygu Ceylan. Track4gen: Teaching video diffusion models to track points improves video generation. In *Proceedings of the Computer Vision and Pattern Recognition Conference*, pages 7276–7287, 2025. 3

[20] Bernhard Kerbl, Georgios Kopanas, Thomas Leimkühler, and George Drettakis. 3d gaussian splatting for real-time radiance field rendering. *ACM Trans. Graph.*, 42(4):139–1, 2023. 2, 17, 18

[21] Chaehyun Kim, Heeseong Shin, Eunbeen Hong, Heeji Yoon, Anurag Arnab, Paul Hongsuck Seo, Sunghwan Hong, and Seungryong Kim. Seg4diff: Unveiling open-vocabulary segmentation in text-to-image diffusion transformers. *arXiv preprint arXiv:2509.18096*, 2025. 13

[22] Min-Seop Kwak, Junho Kim, Sangdoo Yun, Dongyoon Han, Taekyoung Kim, Seungryong Kim, and Jin-Hwa Kim. Aligned novel view image and geometry synthesis via cross-modal attention instillation. *arXiv preprint arXiv:2506.11924*, 2025. 2

[23] Vincent Leroy, Yohann Cabon, and Jérôme Revaud. Grounding image matching in 3d with mast3r. In *European Conference on Computer Vision*, pages 71–91. Springer, 2024. 16

[24] Lingen Li, Zhaoyang Zhang, Yaowei Li, Jiale Xu, Wenbo Hu, Xiaoyu Li, Weihao Cheng, Jinwei Gu, Tianfan Xue, and Ying Shan. Nvcomposer: Boosting generative novel view synthesis with multiple sparse and unposed images. In *Proceedings of the Computer Vision and Pattern Recognition Conference*, pages 777–787, 2025. 2

[25] Zhengqi Li, Qianqian Wang, Noah Snavely, and Angjoo Kanazawa. Infinitenature-zero: Learning perpetual view generation of natural scenes from single images. In *European conference on computer vision*, pages 515–534. Springer, 2022. 17

[26] Zhimin Li, Jianwei Zhang, Qin Lin, Jiangfeng Xiong, Yanxin Long, Xinchi Deng, Yingfang Zhang, Xingchao Liu, Minbin Huang, Zedong Xiao, Dayou Chen, Jiajun He, Jiahao Li, Wenyue Li, Chen Zhang, Rongwei Quan, Jianxiang Lu, Jiabin Huang, Xiaoyan Yuan, Xiaoxiao Zheng, Yixuan Li, Jihong Zhang, Chao Zhang, Meng Chen, Jie Liu, Zheng Fang, Weiyan Wang, Jinbao Xue, Yangyu Tao, Jianchen Zhu, Kai Liu, Sihuan Lin, Yifu Sun, Yun Li, Dongdong Wang, Mingtao Chen, Zhichao Hu, Xiao Xiao, Yan Chen, Yuhong Liu, Wei Liu, Di Wang, Yong Yang, Jie Jiang, and Qinglin Lu. Hunyuan-dit: A powerful multi-resolution diffusion transformer with fine-grained chinese understanding, 2024. 1, 2, 3, 6, 8, 9, 11, 15, 17, 22, 25

[27] Ce Liu, Jenny Yuen, and Antonio Torralba. Sift flow: Dense correspondence across scenes and its applications. *IEEE Transactions on Pattern Analysis and Machine Intelligence*, 33(5):978–994, 2011. 4, 5, 13, 15, 16, 24

[28] Ruoshi Liu, Rundi Wu, Basile Van Hoorick, Pavel Tokmakov, Sergey Zakharov, and Carl Vondrick. Zero-1-to-3: Zero-shot one image to 3d object. In *Proceedings of the IEEE/CVF international conference on computer vision*, pages 9298–9309, 2023. 2, 5, 6

[29] Ilya Loshchilov and Frank Hutter. Decoupled weight decay regularization. In *7th International Conference on Learning Representations, ICLR 2019*, 2019. 6

[30] David G Lowe. Distinctive image features from scale-invariant keypoints. *International journal of computer vision*, 60(2):91–110, 2004. 13

[31] Yuanxun Lu, Jingyang Zhang, Tian Fang, Jean-Daniel Nahmias, Yanghai Tsin, Long Quan, Xun Cao, Yao Yao, and Shwei Li. Matrix3d: Large photogrammetry model all-in-one. In *Proceedings of the Computer Vision and Pattern Recognition Conference*, pages 11250–11263, 2025. 2, 5, 17

[32] Ben Mildenhall, Pratul P Srinivasan, Matthew Tancik, Jonathan T Barron, Ravi Ramamoorthi, and Ren Ng. Nerf: Representing scenes as neural radiance fields for view synthesis. *Communications of the ACM*, 65(1):99–106, 2021. 2

[33] Jisu Nam, Soowon Son, Dahyun Chung, Jiyoung Kim, Siyoon Jin, Junhwa Hur, and Seungryong Kim. Emergent temporal correspondences from video diffusion transformers, 2025. 3

[34] Alex Nichol, Prafulla Dhariwal, Aditya Ramesh, Pranav Shyam, Pamela Mishkin, Bob McGrew, Ilya Sutskever, and Mark Chen. Glide: Towards photorealistic image generation and editing with text-guided diffusion models. *arXiv preprint arXiv:2112.10741*, 2021. 3

[35] Maxime Oquab, Timothée Darcet, Théo Moutakanni, Huy Vo, Marc Szafraniec, Vasil Khalidov, Pierre Fernandez, Daniel Haziza, Francisco Massa, Alaaeldin El-Nouby, et al. Dinov2: Learning robust visual features without supervision. *arXiv preprint arXiv:2304.07193*, 2023. 2, 6

[36] William Peebles and Saining Xie. Scalable diffusion models with transformers. In *Proceedings of the IEEE/CVF international conference on computer vision*, pages 4195–4205, 2023. 2, 3

[37] Jeremy Reizenstein, Roman Shapovalov, Philipp Henzler, Luca Sbordone, Patrick Labatut, and David Novotny. Common objects in 3d: Large-scale learning and evaluation of real-life 3d category reconstruction. In *International Conference on Computer Vision*, 2021. 2, 6, 7, 8, 13, 15, 16, 17, 20, 24, 25

[38] Robin Rombach, Andreas Blattmann, Dominik Lorenz, Patrick Esser, and Björn Ommer. High-resolution image synthesis with latent diffusion models. In *Proceedings of the IEEE/CVF conference on computer vision and pattern recognition*, pages 10684–10695, 2022. 2, 3, 4, 5, 6, 10, 13, 15, 17, 24

[39] Ruoxi Shi, Hansheng Chen, Zhuoyang Zhang, Minghua Liu, Chao Xu, Xinyue Wei, Linghao Chen, Chong Zeng, and Hao Su. Zero123++: a single image to consistent multi-view diffusion base model. *arXiv preprint arXiv:2310.15110*, 2023. 2, 5

[40] Yichun Shi, Peng Wang, Jianglong Ye, Mai Long, Kejie Li, and Xiao Yang. Mvdream: Multi-view diffusion for 3d generation. *arXiv preprint arXiv:2308.16512*, 2023. 2, 3

[41] Oriane Siméoni, Huy V Vo, Maximilian Seitzer, Federico Baldassarre, Maxime Oquab, Cijo Jose, Vasil Khalidov, Marc Szafraniec, Seungeun Yi, Michaël Ramamonjisoa, et al. Dinov3. *arXiv preprint arXiv:2508.10104*, 2025. 4, 5, 8, 13, 15, 24

[42] Jiaming Song, Chenlin Meng, and Stefano Ermon. Denoising diffusion implicit models. *arXiv preprint arXiv:2010.02502*, 2020. 6, 10

[43] Jianlin Su, Yu Lu, Shengfeng Pan, Ahmed Murtadha, Bo Wen, and Yunfeng Liu. Roformer: Enhanced transformer with rotary position embedding, 2023. 17

[44] Lin Sun, Jiale Cao, Jin Xie, Fahad Shahbaz Khan, and Yanwei Pang. iseg: An iterative refinement-based framework for training-free segmentation. *arXiv preprint arXiv:2409.03209*, 2024. 3

[45] Stanislaw Szymanowicz, Jason Y Zhang, Pratul Srinivasan, Ruiqi Gao, Arthur Brussee, Aleksander Holynski, Ricardo Martin-Brualla, Jonathan T Barron, and Philipp Henzler. Bolt3d: Generating 3d scenes in seconds. *arXiv preprint arXiv:2503.14445*, 2025. 2, 5

[46] Luming Tang, Menglin Jia, Qianqian Wang, Cheng Perng Phoo, and Bharath Hariharan. Emergent correspondence from image diffusion, 2023. 17

[47] Hung-Yu Tseng, Qinbo Li, Changil Kim, Suhib Alsisan, Jia-Bin Huang, and Johannes Kopf. Consistent view synthesis with pose-guided diffusion models. In *Proceedings of the IEEE/CVF Conference on Computer Vision and Pattern Recognition (CVPR)*, pages 16773–16783, 2023. 17

[48] Jianyuan Wang, Minghao Chen, Nikita Karaev, Andrea Vedaldi, Christian Rupprecht, and David Novotny. Vggt: Visual geometry grounded transformer. In *Proceedings of the Computer Vision and Pattern Recognition Conference*, pages 5294–5306, 2025. 2, 3, 4, 5, 6, 13, 15, 16, 24

[49] Shuzhe Wang, Vincent Leroy, Yohann Cabon, Boris Chidlovskii, and Jerome Revaud. Dust3r: Geometric 3d vision made easy. In *Proceedings of the IEEE/CVF Conference on Computer Vision and Pattern Recognition*, pages 20697–20709, 2024. [3](#), [5](#), [15](#), [16](#)

[50] Daniel Watson, William Chan, Ricardo Martin-Brualla, Jonathan Ho, Andrea Tagliasacchi, and Mohammad Norouzi. Novel view synthesis with diffusion models. *arXiv preprint arXiv:2210.04628*, 2022. [2](#), [5](#)

[51] Haoyu Wu, Diankun Wu, Tianyu He, Junliang Guo, Yang Ye, Yueqi Duan, and Jiang Bian. Geometry forcing: Marrying video diffusion and 3d representation for consistent world modeling. *arXiv preprint arXiv:2507.07982*, 2025. [3](#), [6](#), [7](#), [8](#)

[52] Yinghao Xu, Hao Tan, Fujun Luan, Sai Bi, Peng Wang, Jiahao Li, Zifan Shi, Kalyan Sunkavalli, Gordon Wetzstein, Zexiang Xu, and Kai Zhang. Dmv3d: Denoising multi-view diffusion using 3d large reconstruction model, 2023. [10](#)

[53] Mark YU, Wenbo Hu, Jinbo Xing, and Ying Shan. Trajectorycrafter: Redirecting camera trajectory for monocular videos via diffusion models. *arXiv preprint arXiv:2503.05638*, 2025. [2](#)

[54] Sihyun Yu, Sangkyung Kwak, Huiwon Jang, Jongheon Jeong, Jonathan Huang, Jinwoo Shin, and Saining Xie. Representation alignment for generation: Training diffusion transformers is easier than you think. *arXiv preprint arXiv:2410.06940*, 2024. [2](#), [3](#), [6](#), [7](#), [8](#), [15](#)

[55] Jensen Zhou, Hang Gao, Vikram Voleti, Aaryaman Vasishta, Chun-Han Yao, Mark Boss, Philip Torr, Christian Rupprecht, and Varun Jampani. Stable virtual camera: Generative view synthesis with diffusion models, 2025. [2](#), [3](#), [5](#)

[56] Tinghui Zhou, Richard Tucker, John Flynn, Graham Fyffe, and Noah Snavely. Stereo magnification: Learning view synthesis using multiplane images. *ACM Trans. Graph. (Proc. SIGGRAPH)*, 37, 2018. [2](#), [6](#), [7](#), [8](#), [15](#), [16](#), [17](#), [19](#), [22](#), [23](#)